
Classification-by-Components: Probabilistic Modeling of Reasoning over a Set of Components

Sascha Saralajew^{1,*} Lars Holdijk^{1,*} Maike Rees¹ Ebubekir Asan¹ Thomas Villmann^{2,*}

¹Dr. Ing. h.c. F. Porsche AG, Weissach, Germany,
sascha.saralajew@porsche.de

²University of Applied Sciences Mittweida, Mittweida, Germany,
thomas.villmann@hs-mittweida.de

Abstract

Neural networks are state-of-the-art classification approaches but are generally difficult to interpret. This issue can be partly alleviated by constructing a precise decision process within the neural network. In this work, a network architecture, denoted as Classification-By-Components network (CBC), is proposed. It is restricted to follow an intuitive reasoning based decision process inspired by BIEDERMAN’s recognition-by-components theory from cognitive psychology. The network is trained to learn and detect generic components that characterize objects. In parallel, a class-wise reasoning strategy based on these components is learned to solve the classification problem. In contrast to other work on reasoning, we propose three different types of reasoning: positive, negative, and indefinite. These three types together form a probability space to provide a probabilistic classifier. The decomposition of objects into generic components combined with the probabilistic reasoning provides by design a clear interpretation of the classification decision process. The evaluation of the approach on MNIST shows that CBCs are viable classifiers. Additionally, we demonstrate that the inherent interpretability offers a profound understanding of the classification behavior such that we can explain the success of an adversarial attack. The method’s scalability is successfully tested using the IMAGENET dataset.

1 Introduction

Neural Networks (NNs) dominate the field of machine learning in terms of image classification accuracy. Due to their design, considered as black boxes, it is however hard to gain insights into their decision making process and to interpret why they sometimes behave unexpectedly. In general, the interpretability of NNs is under controversial discussion [1–4] and pushed researchers to new methods to improve the weaknesses [5–7]. This is also highlighted in the topic of robustness of NNs against adversarial examples [8]. Prototype-based classifiers like Learning Vector Quantizers [9, 10] are more interpretable and can provide insights into their classification processes. Unfortunately, they are still hindered by their low base accuracies.

The method proposed in this work aims to answer the question of interpretability by drawing inspirations from BIEDERMAN’s theory recognition-by-components [11] from the field of cognitive psychology. Roughly speaking, BIEDERMAN’s theory describes how humans recognize complex objects by assuming that objects can be decomposed into generic parts that operate as structural primitives, called *components*. Objects are then classified by matching the *extracted decomposition plan* with a *class Decomposition Plan* (DP) for each potential object class. Intuitively, the class DPs

* Authors contributed equally.

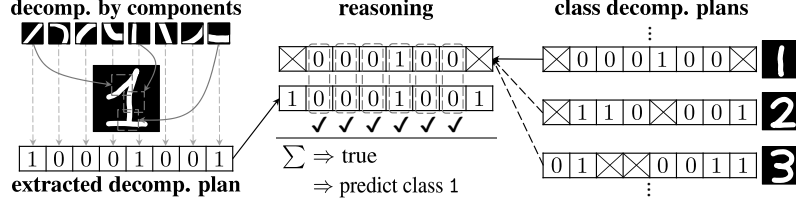


Figure 1: An example realization of the classification process of a CBC on a digit classification task. For simplicity, we illustrate a discrete case where “1” corresponds to detection / positive reasoning, “0” to no detection / negative reasoning, and “ \boxtimes ” to indefinite reasoning.

describe which components are important to be detected and which components are important to not be detected for an object to belong to a specific class. For example, if we consider the classification of a digit as illustrated in Fig. 1, the detection of a component representing a vertical bar provides evidence in favor of the class 1. In other words, we *reason positively* over the vertical bar component for the class 1. Similarly, we can *reason negatively* over all curved components. In contrast to other work on reasoning, the presented approach extends these two intuitive reasoning states by a third type considering *indefinite reasoning*. In Fig. 1, not all components will be important for the recognition of a 1. For instance, we reason neither positively nor negatively over the serif and bottom stroke because not all writing styles use them. In Sec. 2 a network architecture is introduced that models the described classification process in an end-to-end trainable framework such that the components as well as the class DPs can be learned. In line with BIEDERMAN’s theory, we call this a Classification-By-Components network (CBC).

In summary, the contribution of this paper is a classification method, called CBC, with the following important characteristics: (1) The method classifies its input by applying *positive*, *negative*, and *indefinite reasoning* over an extracted DP. To the best of our knowledge, this is the first time that optionality of components/features is explicitly modeled. (2) The method uses a probabilistic reasoning process that directly outputs class hypothesis probabilities without requiring heuristic squashing methods such as softmax. (3) The reasoning process is easily interpretable and simplifies the understanding of the classification decision. (4) The method retains advantages of NNs such as being end-to-end trainable on large scale datasets and achieving high accuracies on complex tasks.

2 The classification-by-components network

In the following we will describe the CBC architecture and how to train it. We present the architecture using full-size components and consecutively generalize this to patch components. Both principles are used in the evaluation in Sec. 4. The architectures are defined (without loss of generality) for vectorial inputs but can be extended to higher dimensional inputs like images.

2.1 Reasoning over a set of full-size components

The proposed framework relies on a probabilistic model based on a probability tree diagram T . This tree T can be decomposed into sub-trees T_c for each class c with the prior class probability $P(c)$ on the starting edge. Such a sub-tree is depicted in Fig. 2. The whole probability tree diagram is modeled over five random variables: c , indicator variable of the class; k , indicator variable of the component; I , binary random variable for importance; R , binary random variable for reasoning by detection; D , binary random variable for detection. The probabilities in the tree T_c are interpreted in the following way: $P(k)$, probability that the k -th component occurs; $P(I|k, c)$, probability that the k -th component is important for the class c ; $P(R|k, c)$, probability that the k -th component has to be detected for the class c ; $P(D|k, \mathbf{x})$, probability that the k -th component is detected in the input \mathbf{x} . The horizontal bar indicates the complementary event, i. e. $P(\bar{D}|k, \mathbf{x})$ is the probability that the k -th component is *not* detected in the input \mathbf{x} . Based on these definitions we derive the CBC architecture.

Extracting the decomposition plan Given an input $\mathbf{x} \in \mathbb{R}^{n_x}$ and a set of trainable *full-size components* $\mathcal{K} = \{\kappa_k \in \mathbb{R}^{n_\kappa} | k = 1, \dots, \#\mathcal{K}\}$ with $n_x = n_\kappa$, the first part of the network detects

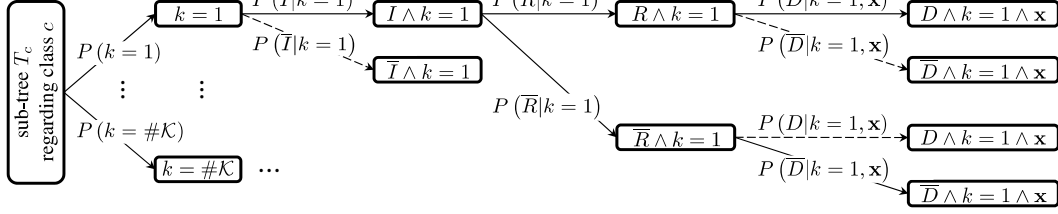


Figure 2: The probability tree diagram T_c that represents the reasoning about one class c . For better readability, the variable of class c is dropped in the mathematical expressions and we only show the full sub-tree for the first component. The solid line paths are the paths of agreement.

the presence of a component κ_k in \mathbf{x} . A feature extractor $\mathbf{f}(\mathbf{x}) = \mathbf{f}(\mathbf{x}; \theta)$ with trainable weights θ takes an input and outputs a feature vector $\mathbf{f}(\mathbf{x}) \in \mathbb{R}^{m_x}$. The feature extractor is used in a Siamese architecture [12] to extract the features of the input \mathbf{x} and of all the components $\{\mathbf{f}(\kappa_k)\}_k$. The extracted features are used to measure the probability $P(D|k, \mathbf{x})$ for the detection of a component by a *detection probability function* $d_k(\mathbf{x}) = d(\mathbf{f}(\mathbf{x}), \mathbf{f}(\kappa_k)) \in [0, 1]$ with the requirement that $\mathbf{f}(\mathbf{x}) = \mathbf{f}(\kappa_k)$ implies $d_k(\mathbf{x}) = 1$. Examples of suitable detection probability functions are the negative exponential over the squared Euclidean distance or the cosine similarity with a suitable handling of its negative part. To finalize the first part of the network, the detection probabilities are collected into the extracted DP as a vector $\mathbf{d}(\mathbf{x}) = (d_1(\mathbf{x}), \dots, d_{\#K}(\mathbf{x}))^T \in [0, 1]^{\#K}$.

Modeling of the class decomposition plans The second part of the network models the class DPs for each class $c \in \mathcal{C} = \{1, \dots, \#C\}$ using the three forms of reasoning discussed earlier. Therefore, we define the *reasoning probabilities*, $r_{c,k}^+$, $r_{c,k}^-$, and $r_{c,k}^0$ as trainable parameters of the model. *Positive reasoning* $r_{c,k}^+ = P(I, R|k, c)$: The probability that the k -th component is important and must be detected to support the class hypothesis c . *Negative reasoning* $r_{c,k}^- = P(I, \bar{R}|k, c)$: The probability that the k -th component is important and must *not* be detected to support the class hypothesis c . *Indefinite reasoning* $r_{c,k}^0 = P(\bar{I}|k, c)$: The probability that the k -th component is not important for the class hypothesis c .² Together they form a probability space and hence $r_{c,k}^+ + r_{c,k}^0 + r_{c,k}^- = 1$. All reasoning probabilities are collected class-wise into vectors $\mathbf{r}_c^+ = (r_{c,1}^+, \dots, r_{c,\#K}^+)^T \in [0, 1]^{\#K}$ and $\mathbf{r}_c^-, \mathbf{r}_c^0$, respectively.

Reasoning We compute the class hypothesis probability $p_c(\mathbf{x})$ regarding the paths of agreement under the condition of importance. An agreement A is a path in the tree T where either a component is detected (D) and requires reasoning by detection (R), or a component is not detected (\bar{D}) and requires reasoning by no detection (\bar{R}). The paths of agreement are marked with solid lines in Fig. 2. Hence, we model $p_c(\mathbf{x})$ by $P(A|I, \mathbf{x}, c)$:

$$P(A|I, \mathbf{x}, c) = \frac{\sum_k (P(R|k, c) P(D|k, \mathbf{x}) + P(\bar{R}|k, c) P(\bar{D}|k, \mathbf{x})) P(I|k, c) P(k)}{\sum_k (1 - P(\bar{I}|k, c)) P(k)}.$$

Substituting by the short form notations for the probabilities, assuming that $P(k) = \frac{1}{\#K}$, and rewriting it with matrix calculus yields

$$p_c(\mathbf{x}) = \frac{(\mathbf{d}(\mathbf{x}))^T \cdot \mathbf{r}_c^+ + (\mathbf{1} - \mathbf{d}(\mathbf{x}))^T \cdot \mathbf{r}_c^-}{\mathbf{1}^T \cdot (\mathbf{1} - \mathbf{r}_c^0)} = (\mathbf{d}(\mathbf{x}))^T \cdot \bar{\mathbf{r}}_c^+ + (\mathbf{1} - \mathbf{d}(\mathbf{x}))^T \cdot \bar{\mathbf{r}}_c^-, \quad (1)$$

where $\mathbf{1}$ is the one vector of dimension $\#K$ and $\bar{\mathbf{r}}_c^\pm$ are the normalized *effective reasoning possibility vectors*. The probabilities for all classes are then collected into the *class hypothesis possibility vector* $\mathbf{p}(\mathbf{x}) = (p_1(\mathbf{x}), \dots, p_{\#C}(\mathbf{x}))^T$ to create the network output. We emphasize that $\mathbf{p}(\mathbf{x})$ is a *possibility vector* as $\sum_c p_c(\mathbf{x}) = 1$ does not necessarily hold. See the supplementary material Sec. B.1 for a detailed derivation of Eq. (1) and Sec. B.2 for a transformation of $\mathbf{p}(\mathbf{x})$ into a class probability vector.

²Note that the idea to explicitly model the state that a component does not contribute and avoid the general probabilistic approach $r_{c,k}^+ = 1 - r_{c,k}^-$ is related to the DEMPSTER-SHAFFER theory of evidence [13].

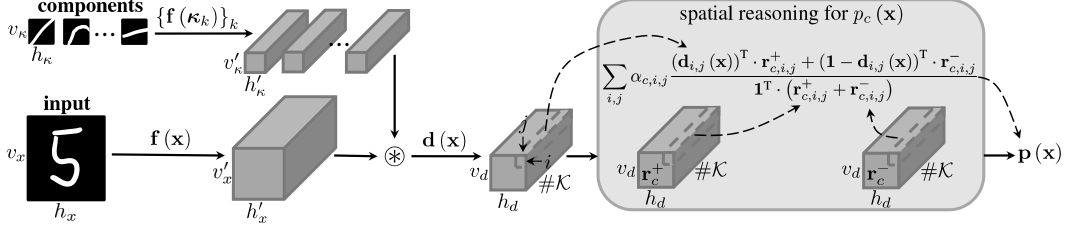


Figure 3: CBC with patch components and spatial reasoning for image inputs.

Training of a CBC We train the networks end-to-end by minimizing the contrastive loss

$$l(\mathbf{x}, y) = \phi(\max\{p_c(\mathbf{x}) \mid c \neq y, c \in \mathcal{C}\} - p_y(\mathbf{x})) \quad (2)$$

where $y \in \mathcal{C}$ is the class label of \mathbf{x} , using stochastic gradient descent learning. The function $\phi : [-1, 1] \rightarrow \mathbb{R}$ is a monotonically increasing, almost everywhere differentiable squashing function. It regulates the generalization-robustness-trade-off over the probability gap between the correct and highest probable incorrect class. This loss is similar to commonly used functions in prototype-based learning [14, 15]. The trainable parameters of a CBC are θ , all $\kappa \in \mathcal{K}$, and \mathbf{r}_c^+ , \mathbf{r}_c^0 , \mathbf{r}_c^- for all $c \in \mathcal{C}$. We refer to the supplementary material Sec. D for detailed information about the training procedure.

2.2 Extension to patch components

Assume the feature extractor \mathbf{f} processes different input sizes down to a minimal (receptive field) dimension of n_0 , similar to most Convolutional NNs (CNNs). To relax the assumption $n_x = n_\kappa$ of full-size components and to step closer to the motivating example of Fig. 1, we use a set \mathcal{K} of trainable *patch components* with $n_x \geq n_\kappa \geq n_0$ such that $\mathbf{f}(\kappa_k) \in \mathbb{R}^{m_\kappa}$ where $m_x \geq m_\kappa$. Moreover, $d_k(\mathbf{x})$ is extended to a sliding operation [16, 17], denoted as \otimes . The result is a *detection possibility stack* (extracted spatial DP) of size $v_d \times \#\mathcal{K}$ where v_d is the spatial dimension after the sliding operation, see Fig. 3 for an image processing CBC. However, Eq. (1) can only handle one detection probability for each component and thus the reasoning process has to be redefined:

Downsampling A simple approach is to downsample the detection possibility stack over the spatial dimension v_d such that the output is a detection possibility vector and Eq. (1) can be applied. This can be achieved by applying global pooling techniques like global max pooling.

Spatial reasoning Another approach is the extension of the reasoning process to work on the spatial DP which we call *spatial reasoning*. For this, the detection possibility stack of size $v_d \times \#\mathcal{K}$ is kept as depicted in Fig. 3. To compute the class hypothesis probabilities $p_c(\mathbf{x})$, Eq. (1) is redefined to be a weighted mean over the reasoning at each spatial position $i = 1, \dots, v_d$. Thereby, $\alpha_{c,i} \in [0, 1]$ with $\sum_i \alpha_{c,i} = 1$ are the (non)-trainable *class-wise pixel probabilities* resembling the importance of each pixel position i . See the supplementary material in Sec. C for a further extension.

3 Related Work

Reasoning in neural networks In its simplest form, one can argue that a NN already yields decisions based on reasoning. If one considers a NN to be entirely similar to a multilayer perceptron, the sign of each weight can be interpreted as either negative or positive reasoning over the corresponding feature. In this case a weight of zero would model indefinite reasoning. However, the use of the Rectified Linear Unit (ReLU) activations forces NNs to be positive reasoning driven only. Nevertheless, this interpretation of the weights is used in interpretation techniques such as Class-Activation-Mapping (CAM) [5], which is similar to heatmap visualizations of CBCs.

Explicit modeling of reasoning The use of components, and the inclusion of the negative and indefinite reasoning can be seen as an extension of the work in [7]. However, CBCs do not rely on the complicated three step training procedure presented in the paper and are built upon a probabilistic reasoning model. In [18] a form of reasoning is introduced similar to the indefinite reasoning state by occluding parts of the learned representation. Their components are, however, modeled in a textual form. In general the reasoning process has slight similarities to ideas mentioned in [19] and the modeling of knowledge via graph structures [20–22].

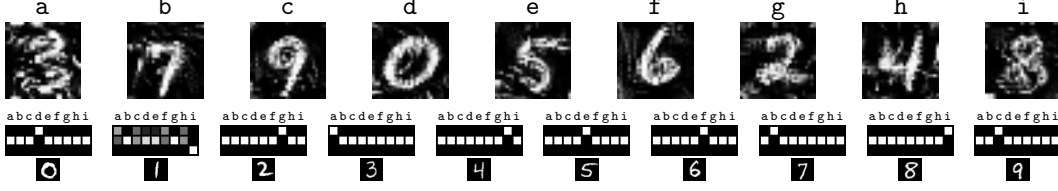


Figure 4: Learned reasoning process of a CBC with 9 components on MNIST. *Top row*: The learned components. *Bottom row*: The learned reasoning probabilities collected in reasoning matrices. The class is indicated by the MNIST digit below. The top row corresponds to $r_{c,k}^+$, middle row to $r_{c,k}^0$, and bottom row to $r_{c,k}^-$. White squares depict a probability of one and black squares of zero.

Feature visualization If the components are defined as trainable parameters in the input space, then the learned components become similar to feature visualization techniques of NNs [23–25]. In contrast, the components are the *direct visualizations of the penultimate layer weights* (detection probability layer), are *not* computed via a post-processing, and have a probabilistic interpretation. Moreover, we are *not* applying regularizations to the components to resemble realistic images.

Prototype-based classification rules and similarity learning A key ingredient of the proposed network is a Siamese architecture to learn a similarity measure [12, 26–28] and the idea to incorporate a kind of prototype-based classification rule into NNs [29–35]. Currently, the prototype³ classification principle is gaining a lot of attention in few-shot learning due to its ability to learn fast from few data [29, 30, 36–38]. The idea to replace prototypes with patches in similarity learning has also been gaining attraction, as can be seen in [39] for the use of object tracking.

4 Evaluation

In this section the evaluation of the CBCs is presented. Throughout the evaluation, interpretability is considered as an important characteristic. In this case, something is interpretable if it has a meaning to experts. We evaluate CBCs on MNIST [40] and IMAGENET [41]. The input spaces are defined over $[0, 1]$ and the datasets are normalized appropriately. Moreover, components that are defined in the input space are constrained to this space as well. The CBCs use the cosine similarity with ReLU activation as detection probability function. They are trained with the *margin loss* defined as Eq. (2) with $\phi(x) = \text{ReLU}(x + \beta)$, where β is a margin parameter, using the Adam optimizer [42]. An extended evaluation including an ablation study regarding the network setting on MNIST is presented in the supplementary material in Sec. E. Where possible, we report mean and standard deviation of the results. The source code is available at www.github.com/saralajew/cbc_networks.

4.1 MNIST

The CNN feature extractors are implemented without the use of batch normalization [43], with Swish activation [44], and the convolutional filters constraint to a Euclidean norm of one. We trained the components and reasoning probabilities from scratch using random initialization. Moreover, the margin parameter β was set to 0.3.

4.1.1 Negative reasoning: Beyond the best matching prototype principle

The CBC architecture in this experiment uses a 4-layer CNN feature extractor and full-size components. During the ablation study we found that in nearly all cases this CBC with 10 components converged to the Best Matching Prototype Principle (BMPP) [45] and formed prototypical components. This means that the reasoning for one class is performed with only strong positive reasoning over one and indefinite reasoning over all the other components, e. g. see the reasoning matrix of class 0 in Fig. 4 and the corresponding prototypical component d. To analyze if the network is able to classify using negative reasoning, we restricted the number of components to be smaller than the number of classes.

³In contrast to prototypes, components are *not* class dependent.

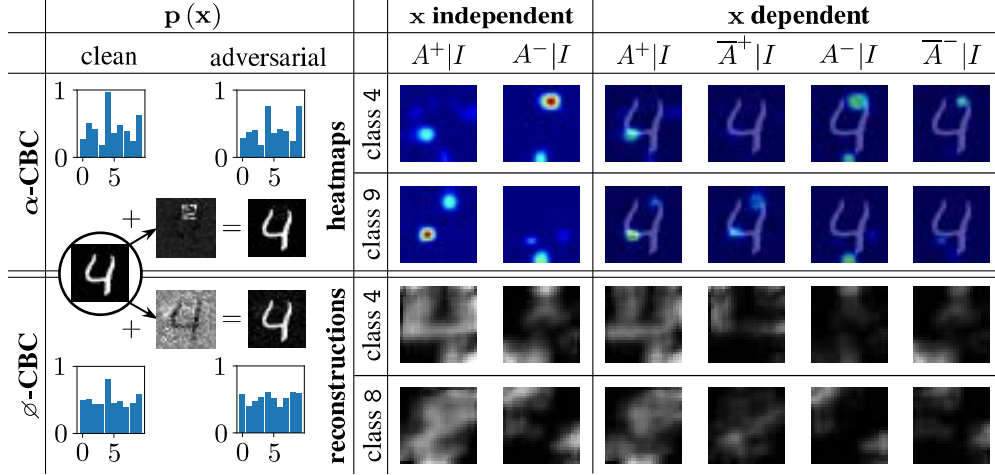


Figure 5: Visualization of the α -CBC heatmaps and the ϕ -CBC reconstructions for an adversarial input. For simplicity, we illustrate the more meaningful visualization for each model. The model visualizations correspond to the best matching reasoning stack regarding the input. We use the color coding “JET” to map probabilities of 0 to blue and 1 to red.

Fig. 4 shows the learned reasoning process of a CBC with 9 components. Similar to the 10 component version, the CBC learns to classify as many classes as possible by the BMPP. In the example, these are all classes except the class 1, for which the CBC uses slightly positive reasoning over the components a, c, f, and h but mostly depends on negative reasoning over component i. This indicates that if an input image is classified as a 1, the network requires it to *not* look like an 8. A comparison of the shapes of the digits 1 and 8 supports this observation, the 8 only consists of curved edges while the 1 does not contain any and on average contains the least white pixels while the 8 requires the most. This result shows that by incorporating the negative and indefinite reasoning state, the CBCs are able to learn both the well understood BMPP and unrestricted approaches beyond the intuitive classification principles by themselves. Both networks achieved close to the state-of-the-art test accuracies over three runs of $(99.32 \pm 0.09)\%$.

4.1.2 Interpretation of the reasoning

In this section we show the interpretability of CBCs. Similar to interpretation techniques from NNs we do this by considering input dependent and input independent visualizations. Moreover, to stress the visualizations in such a way that they really show how the model classifies, we: **(1)** Train two patch component CBCs similar to Fig. 3, one with trainable, denoted as α -CBC, and one with non-trainable pixel probabilities fixed to $\alpha_{c,i,j} = (v_d \cdot h_d)^{-1}$, denoted as ϕ -CBC. **(2)** Generate an adversarial image for both models with the boundary attack [46] and show how they fool the model.

Both CBCs use 8 patch components⁴ of size $v_\kappa, h_\kappa = 7$. The feature extractor is a 2-layer CNN which extracts feature stacks of spatial size $v'_\kappa, h'_\kappa = 1$ and $v'_x, h'_x = 22$. The spatial reasoning size of $v_d, h_d = 7$ was obtained by including a final max pooling operation of pool size 3 in $\mathbf{d}(\mathbf{x})$. Additionally for each class, two reasoning possibility stacks were learned and winner-take-all was applied to determine $p_c(\mathbf{x})$. We call this *multiple reasoning* as we allow the model to learn multiple concepts for each class. The final test accuracies of both models are quasi equivalent and on average over three runs $(97.33 \pm 0.19)\%$. Similar to the previous section, the patch components start to resemble realistic digit parts like strokes, arcs, line-endings, etc.

The interpretability of the CBCs is based on visualizations of how the probability mass is distributed over the tree T . The class hypothesis probability $p_c(\mathbf{x})$, see Eq. (1), is the probability of *agreement under the condition of importance*, denoted by $A|I$. This event describes the correct matching of the extracted and class DP. Moreover, we decompose this event into the positive and negative reasoning part: *Positive* $A|I$ is the event that a component is detected that should be detected and is denoted by $A^+|I$. *Negative* $A|I$ is the event that a component that should not be detected is not detected and is

⁴The idea is to learn patches of: four quarters of a circle plus two diagonal, horizontal, and vertical lines.

denoted by $A^-|I$. Both events can be related to paths in the trees T_c from the root to the leaves, i. e. $A^+|I$ is the upper solid line path and $A^-|I$ is the lower solid line path in Fig. 2. The probability of $A|I$ can be thought of as evidence in favor of a class. Similarly, we can consider the complementary event of $A|I$ which is *disagreement under the condition of importance*, denoted by $\bar{A}|I$, and occurs when the extracted DP does not match the class DP. Again, this occurs either as *positive* $\bar{A}|I$ when a component over which the CBC reasons positively is not detected, denoted by $\bar{A}^+|I$, or as *negative* $\bar{A}|I$ when a component with negative reasoning is detected, denoted by $\bar{A}^-|I$. The related paths in the tree T_c in Fig. 2 are the dashed line paths excluding non-importance. In general, the probability of $\bar{A}|I$ is evidence against a class.

Accordingly to Eq. (1), the visualizations are based on the probabilities in the tree T for respective detection possibility vectors $\mathbf{z}_{i,j}$. These probabilities are collected into the following possibility vectors:⁵ $\mathbf{z}_{i,j} \circ \bar{\mathbf{r}}_{c,i,j}^+$ for $A^+|I$; $(\mathbf{1} - \mathbf{z}_{i,j}) \circ \bar{\mathbf{r}}_{c,i,j}^+$ for $\bar{A}^+|I$; $(\mathbf{1} - \mathbf{z}_{i,j}) \circ \bar{\mathbf{r}}_{c,i,j}^-$ for $A^-|I$; $\mathbf{z}_{i,j} \circ \bar{\mathbf{r}}_{c,i,j}^-$ for $\bar{A}^-|I$. Moreover, we collect all the possibility vectors of one event for all i, j in a stack. Using such a stack we create the visualizations by three procedures: **Probability heatmaps:** Upsample a stack to the input size and sum over k . This visualizes the probabilities for the respective event at the certain position. **Reconstructions:** Upsample a stack to $v'_x \times h'_x \times \#\mathcal{K}$, scale each patch component κ_k by the respective probability and draw them onto an initially black image of size $v_x \times h_x$ at the respective position. After a normalization step, the resulted reconstruction image gives an impression of the combination of the patches that is used to classify the image. **Incorporation of pixel probabilities:** Upsample the class-wise pixel probability maps α_c to $v_x \times h_x$ and normalize by the maximal value such that the most important pixels have a value of one. This map is finally overlaid over the heatmaps and reconstructions to highlight the impact of each pixel to the overall classification decision.

Input independent interpretation Input independent interpretations are calculated by setting $\mathbf{z}_{i,j}$ to the optimal vector with 1 for positive and for 0 negative $A|I$. They provide an answer to the question: “What has the model learned about the dataset?”, see Fig. 5 “x independent”. For both models, the learned concepts of the clean and adversarial class are visualized by the optimal $A^+|I$ and $A^-|I$. As visible in the heatmaps, the α -CBC learned to recognize only as few parts as needed to distinguish the two classes. In case of the 4, this consists of a check that there is no stroke at the bottom and top, see $A^-|I$, while there is a corner on the left, see $A^+|I$. Such a radical sparse coding is learned for all classes. The reasoning for the 9 is similar except that it requires $A^+|I$ instead of $A^-|I$ for the top stroke. In contrast, the \emptyset -CBC learned the whole concept for digits and not just a sparse coding as the reconstructions show real digit shapes in the $A^+|I$. Moreover, the model performs interpretable “sanity checks” via $A^-|I$, e. g. no top stroke at the 4.

Input dependent interpretation Input dependent interpretations are obtained by setting $\mathbf{z}_{i,j}$ to $\mathbf{d}_{i,j}(\mathbf{x})$. To understand why the adversarial images fool the models by human imperceptible “noise” we answer the following question: “Which parts of the input provide evidence for/against the current classification decision?”, see Fig. 5 “x dependent”. By considering the clean probability histogram $\mathbf{p}(\mathbf{x})$ of the α -CBC we see that the clean input perfectly fits the learned concept of a 4 as it had a probability of 1. The adversarial attack has turned the input into a 4 and 9 at the same time, see adversarial $\mathbf{p}(\mathbf{x})$. Remarkably, the attack found the high similarity between the two learned concepts and attacks the model by highlighting a few pixels in the top bar region in form of a patch – the manipulation only changes one pixel in $\mathbf{d}(\mathbf{x})$. Hence, the concept of a 4 is slightly violated as we see a highlighting of the top stroke region in the $\bar{A}^+|I$. This causes the probability drop of the class 4. At the same time, these few pixels provide $A^+|I$ for the top stroke of a 9 and, hence, raise the probability. For the \emptyset -CBC, the attack behavior is totally different. Since the clean input already does not match the learned concept perfectly as $p_4(\mathbf{x}) \approx 0.8$, the attack fools the model by reducing the contrast via background noise. For example, via the $\bar{A}^+|I$ the model highlights that the clear detection of the upper part of the 4 is not given. Moreover, it recognizes that there could be a top/bottom stroke, see $\bar{A}^-|I$. A similar interpretation holds for the adversarial class.

⁵The symbol “ \circ ” denotes the Hadamard product (element-wise multiplication).



Figure 6: The 10 components with the highest $r_{c,k}^+$ for three different classes in the IMAGENET dataset. From top to bottom the classes are: dalmatian, giant panda, and trolleybus. Below each component the $r_{c,k}^+$ (rounded to two digits) is given with respect to the class in question.

Overall result The \varnothing -CBC with $\alpha_{c,i,j} = (v_d \cdot h_d)^{-1}$ is trained to learn a strong concept as it can only reach $p_y(\mathbf{x}) \approx 1$ if it reasons perfectly at *each* pixel position. Therefore, the probability histogram shows a relatively high base probability for all classes, as the overlap between encoded digits to a spatial size of $v_d, h_d = 7$ is often around 50%. Moreover, this restrictive classification principle violates the motivating example in Fig. 1 as the model cannot apply indefinite reasoning over a pixel region. In contrast, the α -CBC is capable of modeling the motivating example but is at the same time a clear example of what happens if we optimize without any constraints as usually performed in NNs. Since the model is trained by minimizing an energy function, it learns to classify correctly with the lowest effort and, hence, oversimplifies. Therefore, the classification will be performed in a non-intuitive way. Moreover, the interpretation shows that the classification of both CBCs is based on non-robust features of \mathbf{f} as both are highly sensitive to background manipulations.

4.2 IMAGENET

To evaluate CBCs on more complex data, we trained a CBC on the IMAGENET dataset. The CBC trained on IMAGENET was implemented using a pre-trained ResNet-50 [47] as *non-trainable* feature extractor. In contrast to the CBCs discussed earlier, the patch components of shape $m_\kappa = 2 \times 2 \times 2048$ are defined *directly* in the feature space. This removes the relation between the components and the input space but drastically improves training time. After downsampling the detection possibility stack of size $v_d, h_d = 6$ by global max pooling, the reasoning is applied, see Sec. 2.2. The components were initialized by cropping the center of 5 images from each class and consecutively processing them through the feature extractor, resulting in 5 000 patch components. If the component k was initialized by a sample from the class c , then we initialized $r_{c,k}^+$ as a uniform random value of $[z, 1]$ where $z = 0.75$ and as a uniform random value of $[0, 1 - z]$ otherwise. Afterwards, the initialization of $r_{c,k}^-$ was determined by $r_{c,k}^+ \cdot (1 - r_{c,k}^+)$. Hence, we biased the model with positive reasoning to components that were sampled from the respective class. The CBC was trained with the margin loss and $\beta = 0.1$. In compliance with earlier work on IMAGENET the input images were rescaled, by first rescaling the shortest side to 224 and then performing a center cropping of size 224×224 . For the same reason no image augmentation was used.

Interpretability In Fig. 6 the 10 components with the highest positive reasoning probabilities for three exemplary classes are presented. After training the components in the feature space, the input representation of the components is determined by searching for the highest detection probability in the training set for the given component and cropping the corresponding image area in the input space. This method is similar to the approach from [7]. In general, the components with a high positive reasoning factor (above the initialization bound of z) are found to be conceptually meaningful for the respective class. Further investigation of the components shows that the detection of the component with the second highest positive reasoning probability for the dalmatian class in an image also provides evidence in favor of the giant panda class. Similarly, the component with the fifth highest positive reasoning probability for the dalmatian class is also highly important for the classes hyena, snow leopard, and english setter while the component with the fifth highest

positive reasoning probability for the class `trolleybus` is also important for the class `trolley car`. Similar shared components can be found across many classes and shows that the CBC is capable of learning complex class independent structures.

Averaged across all classes a positive reasoning probability greater than z was learned for 5.2 ± 0.8 components per class while a negative reasoning probability greater than z was assigned to 2781.8 ± 23.3 out of 5000 components. As can be seen in Fig. 6, in most cases the positive reasoning probabilities assigned to components are close to 1.00. This includes components that were not initialized with a bias towards the class in question. For example, the component with the fifth highest positive reasoning probability for the `dalmatian` class was initially biased towards the `english setter` class. The ratio between the number of positive and negative reasoning components suggest that the model heavily relies on negative reasoning to establish a baseline for its classification decision. We hypothesize that in this higher dimensional setting with a large number of components positive reasoning is primarily utilized to fine tune the models classification decision after rough categorization by negative reasoning.

Performance To evaluate the performance of CBCs, we compare both the accuracy and inference time to that of a CNN. The resulting CBC had an inference time of (371 ± 6) images/sec, similar to (369 ± 2) images/sec of a normal ResNet-50 with global average pooling and fully-connected layer. This shows that the CBC generates no significant computational overhead. The top-5 validation accuracy of 82.4% is on par with earlier CNN generations such as AlexNet with 82.8% [48]. Note that the used CBC had a non-trainable feature extractor and no parameter tuning was performed. We are confident that the accuracy of CBCs on IMAGENET can be improved with further studies. The CBC was evaluated using one NVIDIA Tesla V100 32 GB GPU.

5 Conclusion and outlook

In this paper we have presented a probabilistic classification model called classification-by-components network together with several possible realizations. Boiling down to the essential change we made, this is the definition of a probabilistic framework for the final and penultimate layer of a NN. The detection probability layer is an extension of a convolution layer with the requirement to measure the detection of convolutional filters called components, expressed in probabilities. Moreover, the final reasoning layer is still linear but follows a special implicit constraint defined by the probability model. The overall output is a probability value for each class without any artificial squashing. Independently of the feature extractor used in the CBC, we can always take advantage of this relation during inference by redefining the network to a single feedforward NN such that almost no computational overhead is created. This is shown in the experiment on IMAGENET.

Depending on the training setup, the method inherently contains a lot of different interpretation properties which are all founded on the new probability framework. As shown in the MNIST experiments with Siamese architectures, the method can produce human understandable components and is able to converge to the BMPP without any explicit regularization. Additionally, we have shown that the models can answer questions about the classification decision by an experiment with patch components on MNIST. More precisely, the model shows what causes the failure on an adversarial example. The conclusion drawn here supports the recently published results in [49]. A drawback of the Siamese architecture is the training overhead and the potential introduction of a lot of parameters due to components in the input space. In the non Siamese training, CBCs have almost no downsides to NNs. To be able to use all the presented interpretation techniques, the back projection strategy presented in [7] can be applied, as we have shown on IMAGENET. The evaluation on IMAGENET also showed that CBCs are capable of learning high dimensional components that can be utilized by multiple classes. Investigation of these shared components can provide additional insight into the model’s classification approach. The heatmap visualizations are always applicable and extend the familiar CAM method by the option to visualize disagreement.

The CBC is a promising new method for classification and motivates further research. An initial robustness evaluation and the use of the class hypothesis possibility vectors for outlier detection show promising results, see supplementary material in Sec. E.2.4. Nevertheless, the following remain unanswered: What are proper regularizations for $\alpha_{c,i}$? What are more suitable detection probability functions? What are the advantages of the explicit injection of knowledge into the network in the form of trainable or non-trainable components, as we partly applied in the IMAGENET experiment?

Acknowledgements

We would like to thank Peter Schlicht and Jacek Bodziony from Volkswagen AG, Jensun Ravichandran from the University of Applied Sciences Mittweida, and Frank-Michael Schleif from the University of Applied Sciences Würzburg-Schweinfurt for their valuable input on previous versions of the manuscript. We would also like to thank the whole team at the Innovation Campus from Porsche AG, especially Emilio Oldenziel, Philip Elspas, Mathis Brosowsky, Simon Isele, Simon Mates, and Sebastian Söhner for their continued support and input. Lastly, we would like to thank our attentive anonymous reviewers whose comments have greatly improved this manuscript.

References

- [1] B. M. Lake, T. D. Ullman, J. B. Tenenbaum, and S. J. Gershman. Building machines that learn and think like people. *Behavioral and Brain Sciences*, 40, 2017.
- [2] J. Adebayo, J. Gilmer, M. Muelly, I. Goodfellow, M. Hardt, and B. Kim. Sanity checks for saliency maps. In *Advances in Neural Information Processing Systems*, pages 9505–9515, 2018.
- [3] R. Geirhos, P. Rubisch, C. Michaelis, M. Bethge, F. A. Wichmann, and W. Brendel. ImageNet-trained CNNs are biased towards texture; increasing shape bias improves accuracy and robustness. In *International Conference on Learning Representations*, 2019.
- [4] C. Rudin. Stop explaining black box machine learning models for high stakes decisions and use interpretable models instead. *Nature Machine Intelligence*, 1(5):206, 2019.
- [5] B. Zhou, A. Khosla, A. Lapedriza, A. Oliva, and A. Torralba. Learning deep features for discriminative localization. In *Proceedings of the IEEE Conference on Computer Vision and Pattern Recognition*, pages 2921–2929, 2016.
- [6] Y. Gal and Z. Ghahramani. Dropout as a Bayesian approximation: Representing model uncertainty in deep learning. In *International Conference on Machine Learning*, pages 1050–1059, 2016.
- [7] C. Chen, O. Li, C. Tao, A. J. Barnett, J. Su, and C. Rudin. This looks like that: Deep learning for interpretable image recognition. *arXiv preprint arXiv:1806.10574*, 2018.
- [8] I. Goodfellow, J. Shlens, and C. Szegedy. Explaining and harnessing adversarial examples. In *International Conference on Learning Representations*, 2015.
- [9] J. Bien and R. Tibshirani. Prototype selection for interpretable classification. *The Annals of Applied Statistics*, 5(4):2403–2424, 2011.
- [10] M. Biehl, B. Hammer, and T. Villmann. Prototype-based models in machine learning. *Wiley Interdisciplinary Reviews: Cognitive Science*, 7(2):92–111, 2016.
- [11] I. Biederman. Recognition-by-components: A theory of human image understanding. *Psychological review*, 94(2):115, 1987.
- [12] J. Bromley, I. Guyon, Y. LeCun, E. Säckinger, and R. Shah. Signature verification using a "Siamese" time delay neural network. In *Advances in Neural Information Processing Systems*, pages 737–744, 1994.
- [13] G. Shafer. *A mathematical theory of evidence*, volume 42. Princeton university press, 1976.
- [14] A. Sato and K. Yamada. Generalized Learning Vector Quantization. In *Advances in Neural Information Processing Systems*, pages 423–429, 1996.
- [15] K. Crammer, R. Gilad-Bachrach, A. Navot, and A. Tishby. Margin analysis of the LVQ algorithm. In *Advances in Neural Information Processing Systems*, pages 479–486, 2003.
- [16] Kamaledin Ghiasi-Shirazi. Generalizing the convolution operator in convolutional neural networks. *Neural Processing Letters*, pages 1–20, 2019.

- [17] Sascha Saralajew, Lars Holdijk, Maike Rees, and Thomas Villmann. Prototype-based neural network layers: incorporating vector quantization. *arXiv preprint arXiv:1812.01214*, 2018.
- [18] P. Tokmakov, Y.-X. Wang, and M. Hebert. Learning compositional representations for few-shot recognition. *arXiv preprint arXiv:1812.09213*, 2018.
- [19] Z. Akata, F. Perronnin, Z. Harchaoui, and C. Schmid. Label-embedding for attribute-based classification. In *Proceedings of the IEEE Conference on Computer Vision and Pattern Recognition*, pages 819–826, 2013.
- [20] K. Marino, R. Salakhutdinov, and A. Gupta. The more you know: Using knowledge graphs for image classification. In *Proceedings of the IEEE Conference on Computer Vision and Pattern Recognition*, pages 2673–2681, 2017.
- [21] C. Jiang, H. Xu, X. Liang, and L. Lin. Hybrid knowledge routed modules for large-scale object detection. In *Advances in Neural Information Processing Systems*, pages 1559–1570, 2018.
- [22] X. Chen, L.-J. Li, L. Fei-Fei, and A. Gupta. Iterative visual reasoning beyond convolutions. In *Proceedings of the IEEE Conference on Computer Vision and Pattern Recognition*, pages 7239–7248, 2018.
- [23] D. Erhan, Y. Bengio, A. Courville, and P. Vincent. Visualizing higher-layer features of a deep network. *University of Montreal*, 1341(3):1, 2009.
- [24] M. D. Zeiler and R. Fergus. Visualizing and understanding convolutional networks. In *European Conference on Computer Vision*, pages 818–833. Springer, 2014.
- [25] A. Nguyen, J. Yosinski, and J. Clune. Understanding neural networks via feature visualization: A survey. *arXiv preprint arXiv:1904.08939*, 2019.
- [26] S. Chopra, R. Hadsell, and Y. LeCun. Learning a similarity metric discriminatively, with application to face verification. In *Proceedings of the IEEE Conference on Computer Vision and Pattern Recognition*, pages 539–546, 2005.
- [27] R. Salakhutdinov and G. Hinton. Learning a nonlinear embedding by preserving class neighbourhood structure. In *Artificial Intelligence and Statistics*, pages 412–419, 2007.
- [28] G. Koch, R. Zemel, and R. Salakhutdinov. Siamese neural networks for one-shot image recognition. In *International Conference on Machine Learning – Deep Learning Workshop*, 2015.
- [29] T. Mensink, J. Verbeek, F. Perronnin, and G. Csurka. Metric learning for large scale image classification: Generalizing to new classes at near-zero cost. In *European Conference on Computer Vision*, pages 488–501. Springer, 2012.
- [30] J. Snell, K. Swersky, and R. Zemel. Prototypical networks for few-shot learning. In *Advances in Neural Information Processing Systems*, pages 4077–4087, 2017.
- [31] O. Li, H. Liu, C. Chen, and C. Rudin. Deep learning for case-based reasoning through prototypes: A neural network that explains its predictions. In *Thirty-Second AAAI Conference on Artificial Intelligence*, 2018.
- [32] N. Papernot and P. McDaniel. Deep k-nearest neighbors: Towards confident, interpretable and robust deep learning. *arXiv preprint arXiv:1803.04765*, 2018.
- [33] H.-M. Yang, X.-Y. Zhang, F. Yin, and C.-L. Liu. Robust classification with convolutional prototype learning. In *Proceedings of the IEEE Conference on Computer Vision and Pattern Recognition*, pages 3474–3482, 2018.
- [34] T. Plötz and S. Roth. Neural nearest neighbors networks. In *Advances in Neural Information Processing Systems*, pages 1093–1104, 2018.
- [35] S. O. Arik and T. Pfister. Attention-based prototypical learning towards interpretable, confident and robust deep neural networks. *arXiv preprint arXiv:1902.06292*, 2019.

- [36] O. Vinyals, C. Blundell, T. Lillicrap, K. Kavukcuoglu, and D. Wierstra. Matching networks for one shot learning. In *Advances in Neural Information Processing Systems*, pages 3630–3638, 2016.
- [37] A. Santoro, S. Bartunov, M. Botvinick, D. Wierstra, and T. Lillicrap. Meta-learning with memory-augmented neural networks. In *International Conference on Machine Learning*, pages 1842–1850, 2016.
- [38] S. Gidaris and N. Komodakis. Dynamic few-shot visual learning without forgetting. In *Proceedings of the IEEE Conference on Computer Vision and Pattern Recognition*, pages 4367–4375, 2018.
- [39] L. Bertinetto, J. Valmadre, J. F. Henriques, A. Vedaldi, and P. H. S. Torr. Fully-convolutional siamese networks for object tracking. In *European Conference on Computer Vision*, pages 850–865. Springer, 2016.
- [40] Y. LeCun, C. Cortes, and C. J.C. Burges. The MNIST database of handwritten digits. 1998. <http://yann.lecun.com/exdb/mnist/>.
- [41] J. Deng, W. Dong, R. Socher, L.-J. Li, K. Li, and L. Fei-Fei. ImageNet: A large-scale hierarchical image database. In *Proceedings of the IEEE Conference on Computer Vision and Pattern Recognition*, pages 248–255, 2009.
- [42] D. P. Kingma and J. L. Ba. Adam: A method for stochastic optimization. *arXiv preprint arXiv:1412.6980*, 2014.
- [43] S. Ioffe and C. Szegedy. Batch normalization: Accelerating deep network training by reducing internal covariate shift. In *International Conference on Machine Learning*, pages 448–456, 2015.
- [44] P. Ramachandran, B. Zoph, and Q. V. Le. Searching for activation functions. *arXiv preprint arXiv:1710.05941*, 2017.
- [45] T. Villmann, A. Bohnsack, and M. Kaden. Can Learning Vector Quantization be an alternative to SVM and deep learning? - Recent trends and advanced variants of Learning Vector Quantization for classification learning. *Journal of Artificial Intelligence and Soft Computing Research*, 7(1):65–81, 2017.
- [46] W. Brendel, J. Rauber, and M. Bethge. Decision-based adversarial attacks: Reliable attacks against black-box machine learning models. In *International Conference on Learning Representations*, 2018.
- [47] K. He, X. Zhang, S. Ren, and J. Sun. Deep residual learning for image recognition. In *Proceedings of the IEEE Conference on Computer Vision and Pattern Recognition*, pages 770–778, 2016.
- [48] A. Krizhevsky, I. Sutskever, and G. E. Hinton. ImageNet classification with deep convolutional neural networks. In *Advances in Neural Information Processing Systems*, pages 1097–1105, 2012.
- [49] A. Ilyas, S. Santurkar, D. Tsipras, L. Engstrom, B. Tran, and A. Madry. Adversarial examples are not bugs, they are features. *arXiv preprint arXiv:1905.02175*, 2019.
- [50] K. Eykholt, I. Evtimov, E. Fernandes, B. Li, A. Rahmati, C. Xiao, A. Prakash, T. Kohno, and D. Song. Robust physical-world attacks on deep learning visual classification. In *Proceedings of the IEEE Conference on Computer Vision and Pattern Recognition*, pages 1625–1634, 2018.
- [51] D.-A. Clevert, T. Unterthiner, and S. Hochreiter. Fast and accurate deep network learning by Exponential Linear Units (ELUs). In *International Conference on Learning Representations*, 2016.
- [52] T. Salimans and D. P. Kingma. Weight normalization: A simple reparameterization to accelerate training of deep neural networks. In *Advances in Neural Information Processing Systems*, pages 901–909, 2016.

- [53] E. P. Xing, M. I. Jordan, S. J. Russell, and A. Y. Ng. Distance metric learning with application to clustering with side-information. In *Advances in Neural Information Processing Systems*, pages 521–528, 2003.
- [54] A. Globerson and S. T. Roweis. Metric learning by collapsing classes. In *Advances in Neural Information Processing Systems*, pages 451–458, 2006.
- [55] S.-M. Moosavi-Dezfooli, A. Fawzi, and P. Frossard. Deepfool: A simple and accurate method to fool deep neural networks. In *Proceedings of the IEEE Conference on Computer Vision and Pattern Recognition*, pages 2574–2582, 2016.
- [56] N. Carlini and D. Wagner. Towards evaluating the robustness of neural networks. In *2017 IEEE Symposium on Security and Privacy (SP)*, pages 39–57. IEEE, 2017.
- [57] L. Schott, J. Rauber, M. Bethge, and W. Brendel. Towards the first adversarially robust neural network model on MNIST. In *International Conference on Learning Representations*, 2019.
- [58] A. Madry, A. Makelov, L. Schmidt, D. Tsipras, and A. Vladu. Towards deep learning models resistant to adversarial attacks. In *International Conference on Learning Representations*, 2018.
- [59] J. Rauber, W. Brendel, and M. Bethge. Foolbox: A Python toolbox to benchmark the robustness of machine learning models. *arXiv preprint arXiv:1707.04131*, 2017.
- [60] S. Saralajew, L. Holdijk, M. Rees, and T. Villmann. Robustness of Generalized Learning Vector Quantization models against adversarial attacks. In *International Workshop on Self-Organizing Maps*, pages 189–199. Springer, 2019.
- [61] J. Stallkamp, M. Schlipsing, J. Salmen, and C. Igel. Man vs. computer: Benchmarking machine learning algorithms for traffic sign recognition. *Neural Networks*, 32:323–332, 2012.
- [62] A. Krizhevsky and G. Hinton. Learning multiple layers of features from tiny images. techreport, University of Toronto, 2009.

Supplementary material

A List of mathematical symbols

$\mathbf{0}$	zero vector
$\mathbf{1}$	one vector
A	binary random variable for agreement
A^\pm, \bar{A}^\pm	binary random variable for positive and negative (dis)agreement
$\mathbf{a}_c, \mathbf{b}_c$	coding vectors of the reasoning possibility vectors / stacks for class c during training
$\mathbf{a}, \mathbf{a}_p, \mathbf{a}_p^*$	an adversarial attack, an adversarial L^p -attack, worst-case adversarial L^p -attack
$\text{acc-}\mathbf{a}$	adversarial threshold accuracy on the dataset \mathcal{T}
$\text{acc-}\mathbf{a}_p^*$	worst-case adversarial threshold accuracy of L^p -attacks on the dataset \mathcal{T}
$\alpha_{c,i}, \bar{\alpha}_{c,i,j}$	class-wise pixel probabilities
$\tilde{\alpha}_{c,i}, \tilde{\alpha}_{c,i,j}$	encoded class-wise pixel probabilities as elements of \mathbb{R}
β	margin parameter of margin loss
\mathcal{C}	set of all class labels $\{1, \dots, \#\mathcal{C}\}$
$\#\mathcal{C}$	number of classes
c	class label $c \in \mathcal{C}$ or indicator variable of the class
D	binary random variable for detection
$\mathbf{d}(\mathbf{x})$	detection possibility vector / stack given \mathbf{x}
$d_k(\mathbf{x})$	detection probability function for component κ_k given \mathbf{x}
$\delta_{\mathbf{a}}(\mathbf{x}, y)$	adversarial distance of attack \mathbf{a} on the sample (\mathbf{x}, y)
$\text{median-}\delta_{\mathbf{a}}$	median adversarial distance of attack \mathbf{a} on the dataset \mathcal{T}
$\text{median-}\delta_p^*$	worst-case median adversarial distance of L^p -attacks on the dataset \mathcal{T}
\mathbf{f}	feature extractor
h_d	horizontal spatial dimension of a detection possibility stack
h_κ	horizontal spatial dimension of a component κ
h'_κ	horizontal spatial dimension of a component κ after feature extraction
h_p	horizontal spatial dimension of a class hypothesis possibility stack
h_r	horizontal spatial dimension of a reasoning stack
h_x	horizontal spatial dimension of input \mathbf{x}
h'_x	horizontal spatial dimension of input \mathbf{x} after feature extraction
I	binary random variable for importance
\mathcal{K}	set of all components $\{\kappa_1, \dots, \kappa_{\#\mathcal{K}}\}$
$\#\mathcal{K}$	number of components
k	indicator variable of the component
κ	component variable
L^p	p -norm
$l(\mathbf{x}, y)$	loss function given \mathbf{x} and the corresponding class label y

m_{κ}	dimension of a component κ after feature extraction
m_x	dimension of the input \mathbf{x} after feature extraction
n_0	dimension of the receptive field
n_{κ}	dimension of a component κ
n_x	dimension of the input \mathbf{x}
$\mathbf{p}(\mathbf{x})$	class hypothesis possibility vector given \mathbf{x}
$p_c(\mathbf{x})$	class hypothesis probability for class c given \mathbf{x}
$\phi(x)$	squashing function
R	binary random variable for reasoning by detection
$r_{c,k}^+, r_{c,k}^0, r_{c,k}^-$	positive, indefinite and negative reasoning probability of class c and component κ_k
$\mathbf{r}_c^+, \mathbf{r}_c^0, \mathbf{r}_c^-$	positive, indefinite and negative reasoning possibility vector / stack for class c
$\bar{\mathbf{r}}_c^+, \bar{\mathbf{r}}_c^-$	positive and negative effective reasoning possibility vector / stack for class c
σ	scaling parameter in the negative exponential of the Euclidean distance
T, T_c	probability tree diagram, sub-tree of the probability tree diagram regarding class c
\mathcal{T}	dataset
$t_p, t_0, t_2, t_{\infty}$	adversarial threshold parameters for adversarial threshold accuracies
t_y, t_{β}	prediction and margin reject threshold parameter
θ	trainable parameters of the feature extractor \mathbf{f}
v_d	vertical spatial dimension of a detection possibility stack
v_{κ}	vertical spatial dimension of a component κ
v'_{κ}	vertical spatial dimension of a component κ after feature extraction
v_p	vertical spatial dimension of a class hypothesis possibility stack
v_r	vertical spatial dimension of a reasoning stack
v_x	vertical spatial dimension of input \mathbf{x}
v'_x	vertical spatial dimension of input \mathbf{x} after feature extraction
\mathbf{x}	input variable
$\tilde{\mathbf{x}}$	an adversarial example of \mathbf{x}
y	class label of \mathbf{x}
\mathbf{z}	an arbitrary detection possibility vector

B Mathematical derivation of the class probabilities

First, the class hypothesis probabilities $p_c(\mathbf{x})$ of Eq. (1) are derived and their relation to a probability tree diagram T is presented. Afterwards, we show how the class hypothesis *possibility* vector $\mathbf{p}(\mathbf{x})$ can be transformed into a class *probability* vector. The latter is required to use loss functions such as the cross entropy loss.

B.1 Derivation of the class hypothesis probabilities

The proposed framework relies on a probabilistic model based on a probability tree diagram T . This tree T can be decomposed into sub-trees T_c for each class c with the prior class probability $P(c)$ on the starting edge. Such a sub-tree is depicted in Fig. 2. For better readability, we dropped the variable c in the probability tree diagram in Fig. 2, knowing that all probabilities except the ones on the bottom level, depend on c . We keep the class variable in the mathematical derivation below.

The whole probability tree diagram is modeled over five random variables:

- $c \in \{1, \dots, \#\mathcal{C}\}$, indicator variable of the class;
- $k \in \{1, \dots, \#\mathcal{K}\}$, indicator variable of the component;
- I , binary random variable for importance;
- R , binary random variable for reasoning by detection;
- D , binary random variable for detection.

The probabilities in the probability tree diagram are interpreted in the following way:

- $P(k)$, prior probability that the k -th component occurs;
- $P(I|k, c)$ and $P(\bar{I}|k, c)$, probability that the k -th component is important/not important for the class c ;
- $P(R|k, c)$ and $P(\bar{R}|k, c)$, probability that the k -th component has to be detected/not detected for the class c ;
- $P(D|k, \mathbf{x})$ and $P(\bar{D}|k, \mathbf{x})$, probability that the k -th component is detected/not detected in the input \mathbf{x} .

We compute the class hypothesis probability $p_c(\mathbf{x})$ regarding the paths of agreement A under the condition of importance I . An agreement A is a path in the probability tree diagram where either a component is detected (D) and requires reasoning by detection (R), or a component is not detected (\bar{D}) and requires reasoning by no detection (\bar{R}). The paths of agreement are marked with solid lines in Fig. 2. Hence, we model $p_c(\mathbf{x})$ by $P(A|I, \mathbf{x}, c)$:

$$\begin{aligned} P(A|I, \mathbf{x}, c) &= \frac{P(A, I|\mathbf{x}, c)}{P(I|c)}, \\ &= \frac{\sum_k P(A, I|k, \mathbf{x}, c) P(k)}{\sum_k P(I|k, c) P(k)}. \end{aligned}$$

Using the definition of A , the final equation is

$$\begin{aligned} P(A|I, \mathbf{x}, c) &= \frac{\sum_k (P(R, D, I|k, \mathbf{x}, c) + P(\bar{R}, \bar{D}, I|k, \mathbf{x}, c)) P(k)}{\sum_k (1 - P(\bar{I}|k, c)) P(k)}, \\ &= \frac{\sum_k (P(R|k, c) P(D|k, \mathbf{x}) + P(\bar{R}|k, c) P(\bar{D}|k, \mathbf{x})) P(I|k, c) P(k)}{\sum_k (1 - P(\bar{I}|k, c)) P(k)}. \end{aligned} \quad (3)$$

During the training the reasoning probabilities $r_{c,k}^+$, $r_{c,k}^0$, and $r_{c,k}^-$ are learned. They are defined as:

- Positive reasoning: $r_{c,k}^+ = P(I|k, c) P(R|k, c) \dots$ the probability that the k -th component is important and must be detected to support the class hypothesis c .
- Negative reasoning: $r_{c,k}^- = P(I|k, c) P(\bar{R}|k, c) \dots$ the probability that the k -th component is important and must *not* be detected to support the class hypothesis c .
- Indefinite reasoning: $r_{c,k}^0 = P(\bar{I}|k, c) \dots$ the probability that the k -th component is not important for the class hypothesis c .

Adding the relations $P(D|k, \mathbf{x}) = d_k(\mathbf{x})$ and $P(\bar{D}|k, \mathbf{x}) = 1 - d_k(\mathbf{x})$ and assuming that $P(k) = \frac{1}{\#\mathcal{K}}$ leads to⁶

$$P(A|I, \mathbf{x}, c) = \frac{\sum_k \left(r_{c,k}^+ d_k(\mathbf{x}) + r_{c,k}^- (1 - d_k(\mathbf{x})) \right)}{\sum_k (1 - r_{c,k}^-)}. \quad (4)$$

The statement $r_{c,k}^+ + r_{c,k}^0 + r_{c,k}^- = 1$ is obvious, replacing the summations with the derived probabilities:

$$\begin{aligned} P(R|k, c) P(I|k) + P(\bar{R}|k, c) P(I|k, c) + P(\bar{I}|k, c) &= 1, \\ (P(R|k, c) + P(\bar{R}|k, c)) P(I|k, c) + P(\bar{I}|k, c) &= 1. \end{aligned}$$

A reformulation of Eq. (4) with matrix calculus yields Eq. (1).

B.2 Derivation of the class probability vector

For some applications it is useful to have a class probability vector instead of a class hypothesis possibility vector. To achieve this, the class hypothesis probabilities have to be normalized. The normalization into a class probability vector can be achieved by the derivation of the probability for a class c under the condition of an agreement A and importance I

$$\begin{aligned} P(c|A, I, \mathbf{x}) &= \frac{P(c, A, I, \mathbf{x})}{P(A, I, \mathbf{x})}, \\ &= \frac{P(c, A|I, \mathbf{x})}{P(A|I, \mathbf{x})}, \\ &= \frac{P(A|I, \mathbf{x}, c) P(c)}{\sum_{c' \in \mathcal{C}} P(A|I, \mathbf{x}, c') P(c')}, \\ &= \frac{p_c(\mathbf{x}) P(c)}{\sum_{c' \in \mathcal{C}} p_{c'}(\mathbf{x}) P(c')}, \end{aligned} \quad (5)$$

where $P(c)$ is the prior probability of the class c . Hence, the transformation is obtained by dividing class-wise by the sum of all class hypothesis probabilities.

C Partial spatial reasoning

In the following, the most generic model of the presented reasoning process is described. Each reasoning process (spatial reasoning or reasoning over full-size components) defined in the main paper can be derived in terms of this generic model. In the initial description of spatial reasoning, it is assumed that the spatial dimension of the reasoning possibility stack v_r is equivalent to the spatial dimension of the detection possibility stack v_d . In the general case, we relax this assumption to $v_r \leq v_d$. For example in case of image inputs, the detection possibility stack has a dimension of $v_d \times h_d \times \#\mathcal{K}$ and the reasoning possibility stack the dimension of $v_r \times h_r \times \#\mathcal{K}$ with $v_d \geq v_r$ and $h_d \geq h_r$. Now, instead of computing just one class hypothesis probability $p_c(\mathbf{x})$ as in spatial reasoning, we slide the spatial reasoning process of Fig. 3 with the smaller reasoning possibility stack over the detection possibility stack. This results in a class hypothesis probability map of size $v_p \times h_p$. Additionally, we collect the probabilities of all classes into a stack of size $v_p \times h_p \times \#\mathcal{C}$. As a final step we downsample the possibility stack to a class hypothesis possibility vector, e. g. by applying global max pooling.

The idea behind this approach is that we search at different positions for a match of the learned class DP in the extracted DP. Doing so, we can handle local shifts and, hence, detect objects at different positions in general. In this case, the reasoning process is only applied over a part of the detection possibility stack, thus, we call it *partial spatial reasoning*. This operation can be efficiently implemented as the reasoning process Eq. (1) is equivalent to a linear transformation.

⁶We experimented with networks where the priors $P(k)$ were kept as trainable parameters. The assumption that they have to sum up to one was modeled by a softmax squashing. We found no real advantage to keep these parameters trainable. Nevertheless, to do so might be useful when training sparse models or performing a pruning of the components after the training by thresholding over the learned priors.

D Training of classification-by-components networks

Training of the components If defined as trainable parameters in the input space, it is required to constrain the components κ_k to remain in this space. This is achieved by performing a form of projected gradient descent learning, where the components are clipped back into the correct range after each update. If the components are defined as trainable parameters in the feature space, this is not required and they can be trained over \mathbb{R} .

The projected gradient descent learning is used during the experiments on MNIST, CIFAR-10, and GTSRB, where the input space is defined over the interval $[0, 1]$. For the experiment on IMAGENET, no additional constraint is needed as the components are defined in the feature space.

Training of the reasoning possibility vectors One main condition in the CBCs is that the trainable reasoning vectors \mathbf{r}_c^+ , \mathbf{r}_c^0 , and \mathbf{r}_c^- are elements of $[0, 1]^{\#\mathcal{K}}$ and sum up to one, e.g. $\mathbf{r}_c^+ + \mathbf{r}_c^0 + \mathbf{r}_c^- = \mathbf{1}$. This condition is preserved by encoding the three reasoning vectors for each class into two vectors that can be learned. These two vectors are denoted as \mathbf{a}_c and \mathbf{b}_c and are defined to be elements of $[0, 1]^{\#\mathcal{K}}$. The decoding into the reasoning vectors is defined by

$$\begin{aligned}\mathbf{r}_c^+ &= \mathbf{a}_c, \\ \mathbf{r}_c^- &= (\mathbf{1} - \mathbf{a}_c) \circ \mathbf{b}_c, \\ \mathbf{r}_c^0 &= \mathbf{1} - \mathbf{a}_c - (\mathbf{1} - \mathbf{a}_c) \circ \mathbf{b}_c.\end{aligned}$$

During the training of a network the parameters \mathbf{a}_c and \mathbf{b}_c are constrained to $[0, 1]^{\#\mathcal{K}}$ by clipping values outside the interval after each update which can be seen again as a form of projected gradient descent learning. To avoid the computation of \mathbf{r}_c^0 we can substitute $\mathbf{1} - \mathbf{r}_c^0$ in Eq. (1) by $\mathbf{r}_c^+ + \mathbf{r}_c^-$.

Training of the pixel probabilities In the CBCs with spatial reasoning, the class-wise pixel probabilities $\alpha_{c,i}$ are potentially trainable parameters. By definition, it must hold that $\alpha_{c,i} \in [0, 1]$ and $\sum_{i,j} \alpha_{c,i} = 1$. This is preserved by learning encoded parameters $\tilde{\alpha}_{c,i} \in \mathbb{R}$ that can be decoded using a softmax activation

$$\alpha_{c,i} = \frac{\exp(\tilde{\alpha}_{c,i})}{\sum_{i'} \exp(\tilde{\alpha}_{c,i'})}$$

to get the pixel probabilities $\alpha_{c,i}$.

End-to-end learning of a CBC An important observation is that the components are in general *not* equal to any elements of the dataset. This fact is important for the training of CBCs that use a Siamese setup to extract features from both the inputs and the components. Particularly, one path of the Siamese feature extractor processes the input samples and the other processes the components. To solve the classification problem, it is important that the feature extractor is only updated to extract characterizing features from dataset samples and not from the non-dataset samples (the components). Hence, the gradient backflow to the parameters of the feature extractor path, which is responsible for extracting features from the components, has to be stopped. The gradient backflow through this path is only used for updating the components if they are trainable.

While this is a slight deviation from the usual training procedure of a Siamese network, it improves the training of interpretable components significantly and is theoretically grounded.

E Extended evaluation

In this section, we present an extended evaluation on MNIST, GTSRB and CIFAR-10. Before we start, we describe general settings of the CBCs which were used throughout all experiments. After that, we start with MNIST and present the results of the ablation study and some first robustness evaluation results. We continue with GTSRB where we show how a CBC performs on the physical adversarial images from [50]. Finally, we present results on CIFAR-10.

E.1 General training setup and network setting

If not stated differently, all networks were trained with the following setting on a single NVIDIA Tesla V100 32 GB GPU using KERAS⁷ with TENSORFLOW⁸ backend. The input samples were always normalized to the input space defined over $[0, 1]$. If components/prototypes are defined in the input space, then they are constrained to this space. All networks were trained for 150 epochs with the default Adam optimizer from KERAS with an initial learning rate of 0.003. The learning rate was automatically decreased by a factor of 0.9 when the validation loss did not improve for five epochs. We used a batch size of 128 and data augmentation consisting of ± 2 pixels random shifts and $\pm 15^\circ$ random rotations. The loss function of the CBCs was the introduced margin loss with a margin of $\beta = 0.3$. We trained the whole networks from scratch and initialized the reasoning probabilities with $[0, 1]$ and the components with $[0.45, 0.55]$ uniform random noise.⁹ The detection probability function is the cosine similarity with ReLU activation to clip the negative part.

Depending on the performed experiment, different CNNs are used as feature extractor for the CBC. With the exception of the CNN feature extractor used in the IMAGENET experiment, all feature extractors have a few settings in common. Specifically, the convolutional filters in the feature extractor are constrained to have an Euclidean norm of one and are activated by the Swish activation function. Additionally, the feature extractors do not contain any batch normalization. This setting is chosen based on the results of the ablation study presented in Sec. E.2.2. From here on, we will denote this setting of a CNN feature extractor in combination with the margin loss and cosine similarity detection probability function as the *standard setting*. In contrast, when a CNN feature extractor is used that is more in line with common CNN architectures (no convolutional filter constraint, ReLU activation and batch normalization) we will refer to it as the *non-standard setting*. CBCs with the non-standard setting still use the margin loss and cosine similarity detection probability function, if not stated differently.

All networks were trained at least three times. We report the mean and standard deviation of the test accuracy and give notice when a run diverged. Moreover, we do not report early stop accuracies. In addition, we present the average probability gap of a CBC over the test set. The *probability gap* is defined as

$$\max \{p_c(\mathbf{x}) \mid c \in \mathcal{C}\} - \max \{p_{c'}(\mathbf{x}) \mid c' \in \mathcal{C}, c' \neq \arg \max \{p_c(\mathbf{x}) \mid c \in \mathcal{C}\}\}.$$

This value is different from the probability gap (margin) optimized by the margin loss, as the predicted class is not necessarily equivalent to the correct class.

A note about the detection probability function In parallel to the cosine similarity as detection probability function, in a couple of experiments, we studied the use of the Euclidean distance activated by the negative exponential. As stated in [16], the Euclidean distance can be trained in deep NNs if one takes the distribution of the distance (e. g. the χ^2 statistics if the requirements for this distribution are fulfilled) into account. Otherwise, the Euclidean distance together with the negative exponential leads to the vanishing gradients problem. In the evaluations, we tackled this problem by training a scaling parameter $\sigma \in \mathbb{R}_{>0}$ such that the detection probability function becomes

$$d_k(\mathbf{x}) = \exp \left(-\frac{\|\mathbf{f}(\mathbf{x}) - \mathbf{f}(\boldsymbol{\kappa}_k)\|_2^2}{\sigma} \right). \quad (6)$$

Using this approach with the trainable parameter σ , a CBC with the Euclidean distance was able to achieve similar results to a CBC with the cosine similarity. However, the stability of the training was sensitive to the initialization of σ and was prone to diverge. We see this as an indicator for the detection probability function being crucial for the success of the CBCs and therefore consider it as one of the main focus points of further research.

⁷<https://keras.io/>

⁸<https://www.tensorflow.org/>

⁹This is a suboptimal initialization of the components as it does not include any prior knowledge obtained from having access to the dataset before training. Using class-wise means or (partial) samples of the dataset might lead to earlier convergence.

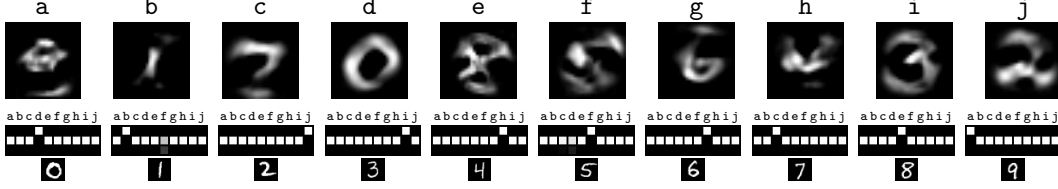


Figure 7: Learned reasoning process of a CBC without feature extractor, 10 components and trained over a margin $\beta = 0.3$ on MNIST. *Top row*: The learned components. *Bottom row*: The learned reasoning probabilities collected in reasoning matrices. The class is indicated by the MNIST digit below. The top row corresponds to $r_{c,k}^+$, middle row to $r_{c,k}^0$, and bottom row to $r_{c,k}^-$. White squares depict a probability of one and black squares of zero.

E.2 MNIST

In this section we present the full evaluation of CBCs with experiments performed on MNIST. The first experiment evaluates the performance of a CBC without a feature extractor on top and compares it to a traditional prototype-based classifier. Following this, we present the results of the ablation study and discuss the impact of certain parameters on the CBC performance. Similar to Sec. 4.1, we use the results of the ablation study to perform a set of experiments with a CBC with feature extractor and a varying number of components. This set of experiments leads to an observation regarding the relation between the interpretability of components and the robustness of the network against adversarial attacks, which we discuss afterwards. Finally, we close this section by presenting additional visualizations and provide an extended description of the construction process of the presented visualizations for patch component CBCs.

E.2.1 CBCs without a feature extractor

Experiment description The purpose of this experiment is to compare the CBC to a prototype-based classifier. Additionally, we want to show that the reasoning process is a natural extension to the BMPP employed by them. For a fair comparison, the identity mapping is used as feature extractor of the CBC. Therefore, the detection probability function computes the dissimilarity directly in the input space (as in most prototype-based classifiers). One of the design goals for the CBC is that the BMPP is a valid solution of the classification process. Therefore, we use an architecture with 10 full-size components, which converges to the BMPP if we train for a robust classification (high enough margin β in the margin loss). Additionally, we show that the CBC can discover an alternative to the BMPP if we allow the classification to be based on weak decisions. This is done by lowering the margin β in the margin loss.

The prototype-based classifier that we compare to the CBC is the Generalized Learning Vector Quantization (GLVQ) method [14] which is a supervised, end-to-end trainable classifier. As baseline, we use GLVQ with one prototype per class and squared Euclidean distance.

Accuracy results In terms of accuracy the CBC performs slightly better than GLVQ with a test accuracy of $(83.5 \pm 0.12) \%$ against $(81.7 \pm 0.22) \%$. If we reduce the margin β to 0.1 the accuracy increases to $(89.5 \pm 0.12) \%$ and clearly outperforms the learned GLVQ model. We hypothesize that the reason for this is that with a smaller margin the network has the freedom to classify by weak decisions. The combined optimization of forcing a margin of 0.3 and high accuracies might result in a trade-off between accuracy and the robustness of the decisions. On the contrary, GLVQ is by design a hypothesis margin maximizer [15]. Thus it is optimizing for a maximal averaged relative margin over all samples and, therefore, forces the model to robust decisions.

Empirical evidence supporting this weak decision hypothesis can be found by evaluating the average probability gap of the CBC classifications. While for a margin of 0.3 this gap is 0.16 ± 0.11 , it is only 0.1 ± 0.05 for a margin of 0.1. For this evaluation only the correct classified images were taken into account and, therefore, the direct comparison to the optimization margin can be made.

Interpretation of the reasoning with a margin of 0.3 In Fig. 7 we depict the learned reasoning process with a margin of $\beta = 0.3$. The network converges consistently towards the BMPP and



Figure 8: Class-specific prototypes learned by GLVQ. The class is indicated by the MNIST digit below.

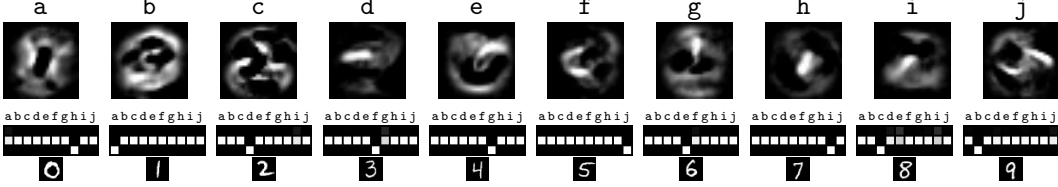


Figure 9: Learned reasoning process of a CBC without a feature extractor, 10 components and trained over a margin $\beta = 0.1$ on MNIST. *Top row*: The learned components. *Bottom row*: The learned reasoning probabilities collected in reasoning matrices. The class is indicated by the MNIST digit below. The top row corresponds to $r_{c,k}^+$, middle row to $r_{c,k}^0$, and bottom row to $r_{c,k}^-$. White squares depict a probability of one and black squares of zero.

turns the class-independent components into prototypical (class-specific) components. The learned components can directly be recognized as class-specific components as they resemble digit shapes. The BMPP is learned if the indefinite reasoning probabilities for all components, except for one, are close to one and if the remaining component is used for positive reasoning. Only for the class 1 the CBC performs a slightly negative reasoning over the component f which can be seen at the grayish negative reasoning probability. It is a remarkable observation that the CBC converges consistently towards the BMPP, without any regularization or constraint over the reasoning process. This behavior shows that the BMPP is a stable solution for a robust classification process. The learned components are similar to the learned prototypes of the GLVQ model in Fig. 8. For example, compare the strong component of class 5 with the learned GLVQ prototype. This provides additional evidence for the claim that a CBC can act similar to a prototype-based classifier, but only if this is the best classification principle for the task. The differences between the learned prototypes and components are the result of the different similarity measures. If we switch to Eq. (6) as detection probability function in the CBC, then the learned components start to become indistinguishable to the learned prototypes.

Interpretation of the reasoning with a margin of 0.1 In contrast to the learned reasoning process with a margin of $\beta = 0.3$, the reasoning process over a low margin is complementary to the BMPP, see Fig. 9. Almost all the decisions are based on strong negative reasoning over one component. Only a few classes show weak positive reasoning over a few components. Hence, the learned components can be interpreted as negative examples of the classes: To make a correct classification of a given image, the strong (negative) component of the correct class should have the lowest detection probability in the image. The interpretation of negative samples is hard as it is not a human intuitive reasoning process.

Albeit a bit less intuitive, it is still possible to understand the classification decision. Consider the reasoning process of the class 0, which relies on strong negative reasoning over component h. This component has a bright dot in the middle and the rest remains almost black. It is not hard to see that this is indeed a negative example for the class 0 as a zero is the only digit which has no stroke in the middle. The same interpretation can be applied for class 1 and the respective component. A more complex interpretation is the reasoning of the class 7 and negative component i. The black top horizontal line indicates a unique property of the seven and a five: the horizontal top stroke. To avoid confusions to a five it strongly highlights the region where a five has the transition from the vertical stroke to the arc – which means this should not be present. The property, that the classification is sometimes based on just finding unique parts and does not understand the whole image, was in general observed in a couple of low margin experiments, also beyond MNIST.

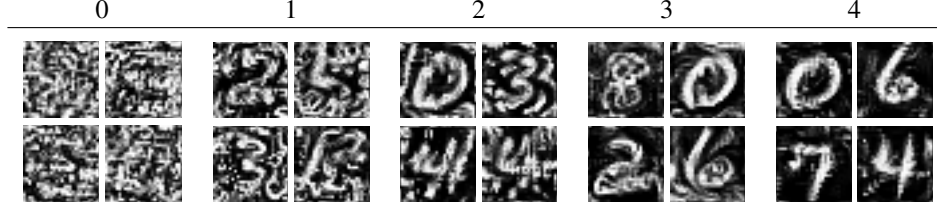


Figure 10: Example components for the visual evaluation of the interpretability. We excluded examples of the score category five as these are assumed as real input images.

E.2.2 Ablation study

As described in Sec. 4.1, we found a strong variation within the interpretability of the components. The goal of this study was to find out how different settings of a CBC effect the interpretability of its components.

Experimental setup The following 4-layer CNN is used as feature extractor for the evaluation:

1. Convolution: 32 filters, kernel size 3×3 , stride 1×1 , bias, no padding;
2. Convolution: 64 filters, kernel size 3×3 , stride 1×1 , bias, no padding;
3. Max pooling: pool size and stride 2×2 ;
4. Convolution: 64 filters, kernel size 3×3 , stride 1×1 , bias, no padding;
5. Convolution: 128 filters, kernel size 3×3 , stride 1×1 , bias, no padding;
6. Max pooling: pool size and stride 2×2 .

The reasoning is defined with 10 full-size components. We experimented with all possible combinations of the following parameters and their configurations (<parameter description: configuration-1, configuration-2, ...>):

- activation function of convolutional layers: ReLU, Swish;
- constraint of convolutional filters (kernels) to Euclidean norm one: true, false;
- application of batch normalization after the first max pooling layer: true, false;
- activation of the cosine similarity to provide the detection probability function: $\text{ReLU}(x)$, $(\text{ReLU}(x))^2$;
- squashing function ϕ in Eq. (2): Exponential Linear Unit (ELU) [51] function, margin loss with $\beta = 0.1$, margin loss with $\beta = 0.3$, margin loss with $\beta = 0.5$, margin loss with $\beta = 0.7$, margin loss with $\beta = 0.9$.

Evaluation After the networks were trained, we extracted the final components for each combination. We asked 10 human experts to give scores to the interpretability of components by visual examination. For each combination, we asked for one score for all resulting components. The score values were described according to the following definitions and accompanied by the examples in Fig. 10:

Score of 0: The images resemble unstructured noise with no visible digit shapes.

Score of 1: The images show something resembling a digit, but the image contains a lot of noise.

Score of 2: The images show something resembling a digit, but might contain artifacts of other digits.

Score of 3: The images show real looking digits, but the background contains a lot of noise.

Score of 4: The images show real looking digits and background contains close to no noise.

Score of 5: The images are indistinguishable from real inputs.

The final interpretability score is computed as the average. Additionally to the interpretation score, we collected some statistics over the training / test accuracy / loss.

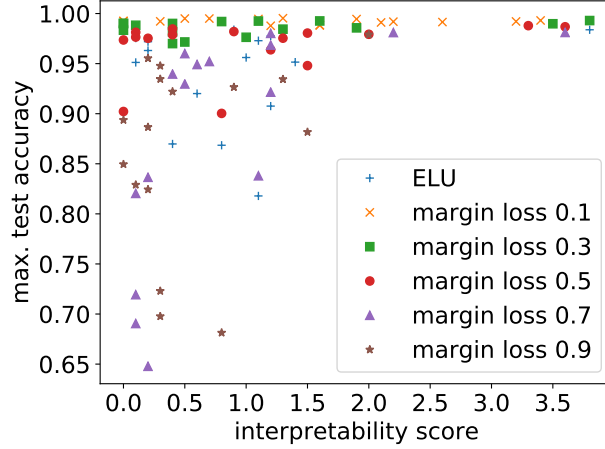


Figure 11: Impact of the squashing function ϕ on the interpretability score and the test accuracy.

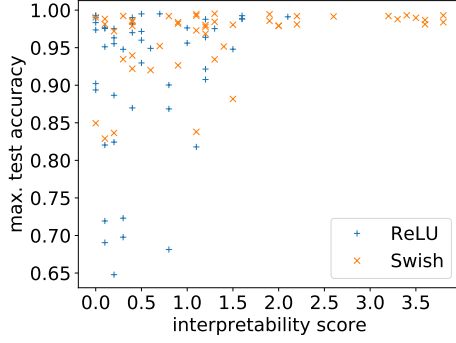
Results Since the overall goal of the ablation study is to find a CBC setting where the components are learned to be human interpretable, the first evaluation criterion is the interpretability score. Two of the combinations scored an interpretability score of 3.8 (the highest score that was given to a model by a single expert was 4). The difference between these two models is the loss function in use, see Fig. 11. The first model was trained with ELU function for ϕ whereas the other model was trained over the margin loss with a margin of $\beta = 0.3$. To decide which model performs better, we compared their final test accuracies. The model with the margin loss performed significantly better: $(99.27 \pm 0.1) \%$ average test accuracy with margin loss and $(97.86 \pm 0.19) \%$ with ELU function. Hence, the combination of this point was chosen to be the *standard setting* for CBCs throughout all experiments. Interestingly, the whole evaluation showed that the accuracy is not correlated with the interpretability score, see Fig. 11. Hence, a model with non-interpretable components was able to reach high accuracies.

In Fig. 12 we visualize the effect of the other parameters. There is no clear trend regarding the cosine similarity activation but a clear trend with respect to the other parameters. The defined standard setting clearly outperforms all others.

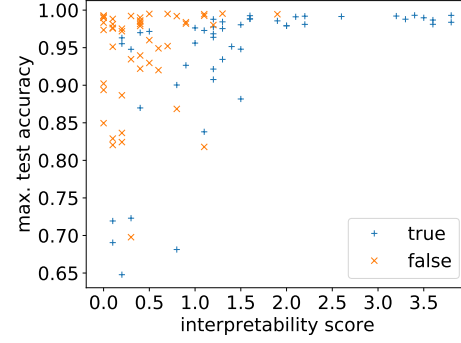
Analysis of the results In general, the Euclidean constraint seems to have the strongest impact on the interpretability, see Fig. 12. We observed the positive effect of this constraint during an experiment with convolutional filters predefined as Sobel operators. The idea behind this constraint is to make all the filters comparable and normalize them in such a way that each can distribute 100% of energy over their weights.¹⁰ Later we realized that in the non-standard setting (ReLU activation of convolutional layers, batch normalization and no constraint), the activations seem to explode with increasing network depth of the feature extractor, see Fig. 13a. Note the different scales of the horizontal axis of the two plots. Independently to that, the CBC with the non-standard setting trained to an acceptable, but lower accuracy of $(98.86 \pm 0.26) \%$ compared to the standard setting. To understand how the network with the non-standard setting classifies, we draw some conclusions from the CBC architecture in use:

1. The cosine similarity is equivalent to a dot product (Euclidean inner product) after the two input vectors were normalized to an Euclidean norm of one.
2. If there are elements in the vector which are order of magnitudes larger than all other elements, then only the largest values will be nonzero after the normalization and only these values can add to a high output similarity.
3. After the normalization, a high detection probability of $d_k(\mathbf{x}) \approx 1$ implies $\frac{\mathbf{f}(\mathbf{x})}{\|\mathbf{f}(\mathbf{x})\|_2} \approx \frac{\mathbf{f}(\kappa_k)}{\|\mathbf{f}(\kappa_k)\|_2}$ and thus the input is similar to the k -th component.

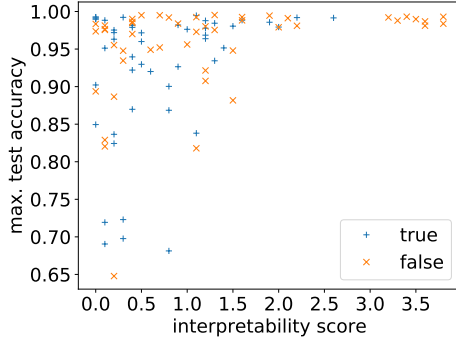
¹⁰In [52], the application of Euclidean normalizations in NNs is studied.



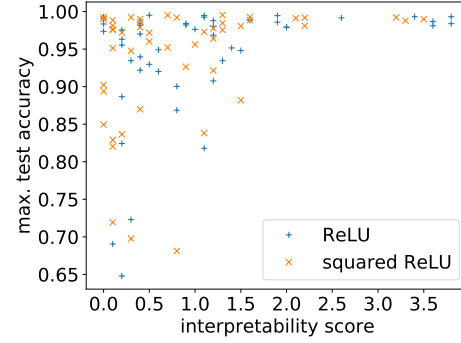
(a) Impact of the activation of convolutional layers on the interpretability score and the test accuracy.



(b) Impact of the Euclidean constraint on the interpretability score and the test accuracy.

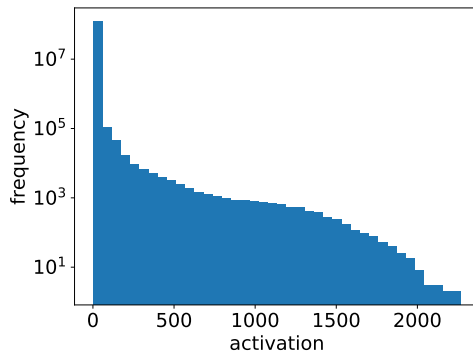


(c) Impact of batch normalization on the interpretability score and the test accuracy.

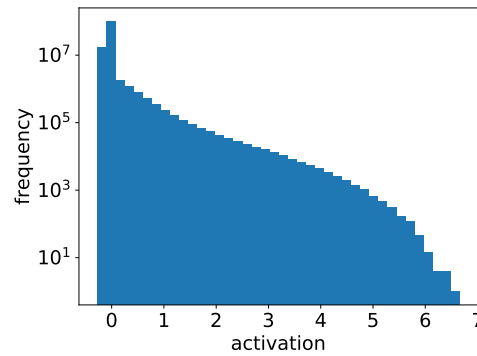


(d) Impact of the cosine similarity activation on the interpretability score and the test accuracy.

Figure 12: The results of the ablation study regarding the parameters convolutional activation, Euclidean constraint, batch normalization and cosine similarity activation.



(a) CBC with non-standard setting.



(b) CBC with the standard setting.

Figure 13: The distribution of the input values (output activations of the feature extractor) to the detection probability function with the non-standard setting (a) and the standard setting (b) depicted as histograms. We evaluated the histograms over the training database.

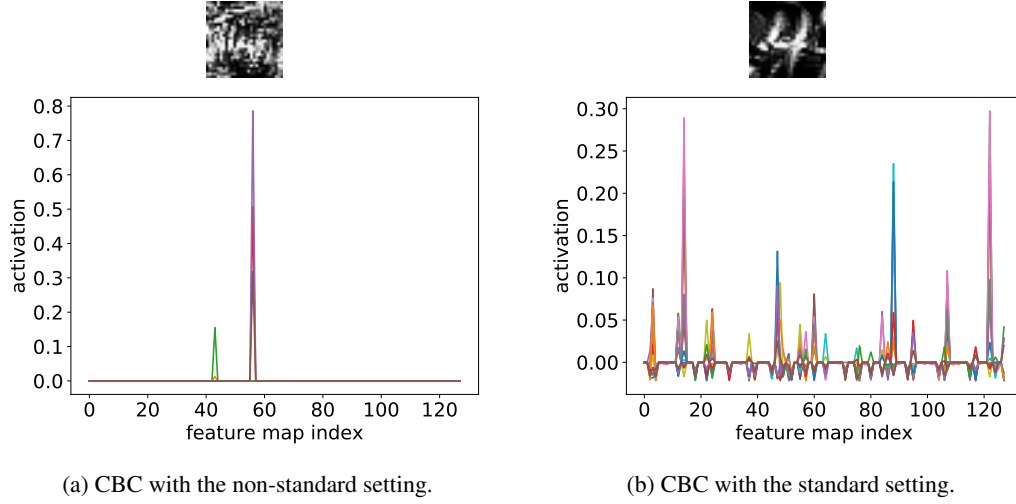


Figure 14: Activations of the feature maps of the final convolutional layer in the feature extractor after Euclidean normalization. The activations are shown for the strong positive component of the class 4 for the non-standard setting (a) and the standard setting (b). The colors within one plot correspond to the spatial dimensions and show how different spatial dimensions within the 4×4 feature stack contribute. Above the plot, the corresponding learned component is depicted.

4. If the model classifies by the BMPP over the prototypical component κ_k for class y and $p_y(\mathbf{x}) \approx 1$ is valid, then $d_k(\mathbf{x}) \approx 1$.

Both networks classify by the BMPP over prototypical components (see Fig. 14 for example components of both networks) with high output probabilities of $p_y(\mathbf{x}) \approx 1$ for correct classifications. The components of the CBC with non-standard setting are not human understandable while the components of the CBC with standard setting are. By conclusion 4 and 3 we know that after the normalization an input has to be approximately equivalent to the strong prototypical component. Moreover, by conclusion 2 we know that only nonzero values contribute to the classification decision.

In case of the non-standard setting, or in other words the setting most often used in CNNs, the nonzero values are those of high activation. Hence, the model outputs high activations to suppress small values. Moreover, the network relies only on a few significant features for each class, see Fig. 14a for an example activation pattern after normalization. The complete classification of a digit four is based on a few features of two different feature maps¹¹. By this “trick” the network does not learn to extract useful features which can be used across the classes but instead amplifies a certain feature map for each class. The activation pattern of a certain class is not understandable as the components can not be interpreted.

With the standard setting the classification works differently. The network cannot overemphasize a few features as the filters are normalized by the Euclidean norm and can also not produce filters where all the weights are zero (“dead” filter). Hence, the network has to incorporate each filter and, therefore, learns highly discriminative features. If we consider the activation patterns across all classes, we observe that the network learns features that are used across multiple classes and that it classifies by combining several features, see the activation pattern after normalization of Fig. 14b. We hypothesize that the reason why the components become human interpretable, is that compared to the network with the non-standard setting, the network with the standard setting really learns to decode the whole digit into a high level representation, such as strokes and arcs. In contrast, the network with the non-standard setting just learns a unique pattern, for example the distribution of intensities.

¹¹A *feature map* is the output produced by one filter of a convolutional layer. Moreover, the *feature map index* refers to the filter index.



Figure 15: Evolution of a component over the epochs of a 10 component CBC.

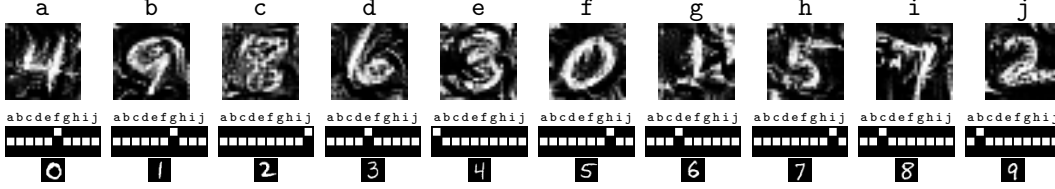


Figure 16: Learned reasoning process of a CBC with 10 components on MNIST. *Top row*: The learned components. *Bottom row*: The learned reasoning probabilities collected in reasoning matrices. The class is indicated by the MNIST digit below. The top row corresponds to $r_{c,k}^+$, middle row to $r_{c,k}^0$, and bottom row to $r_{c,k}^-$. White squares depict a probability of one and black squares of zero.

The different losses show no superior trend regarding a specific setting except that a too big margin in the margin loss is harmful for both interpretability and accuracy. From [53] and [54] we know that the optimization of a similarity (or metric) with a contrastive loss could lead the feature extractor to project all the points from one class to only one single point. This effect is known as collapsing dimensions and is the main reason why we do not apply losses like mean squared error or cross entropy as they rely on the optimization towards a one-hot label. This effect leads to highly non-linear regions in the learned mapping. We believe that the model needs “space” to distribute the feature vectors smoothly and well scattered to converge to the desired interpretability. A compromise between the optimization for correct classifications and the increase of the margin is the ELU squashing. It has a derivative of one for incorrectly classified samples and slowly scales down the updates of already correctly classified images to avoid a collapsing of dimensions. The ELU loss is an alternative to the margin loss and worked well throughout all experiments. However, it is always slightly below the margin loss in terms of accuracy. Moreover, we observe that, even when we are optimizing for a fixed margin of $\beta = 0.3$, the resulting margin is often much bigger, see Fig. 18. This is an indicator that the feature vectors are fairly smoothly distributed throughout the whole space.

So far, we have no explanation for why the batch normalization seems to be harmful for the interpretability. In contrast, we think that the improved behavior of Swish is due to the property that the function is differentiable everywhere and has almost always nonzero gradients.

E.2.3 CBCs with feature extractor

In addition to the results over a 9 component CBC with feature extractor presented in Sec. 4.1.1, in this section we present additional results of a 10 and an 8 components model and show that the CBC can also deal with other numbers of components and still classifies well on MNIST. Afterwards, we show that the sparseness of a CBC (fewer components) does come with reduced performance as the models show a significantly smaller margin between the probabilities of the correct and the incorrect class with the highest probability. This indicates that the models start to classify by weaker decisions. The standard setting for CBCs is used for this experiment, making it equivalent to the 9 component CBC presented in Sec. 4.1.1 but with the different number of components.

10 component CBC To give an impression on how the model learns the components, we present the evolution of a component starting from random noise in Fig. 15. After a few epochs the rough shapes of the modeled digits are visible and the remaining epochs are used for fine-tuning to remove background noise. In general, the training of the model is stable and converges consistently to high test accuracies of $(99.27 \pm 0.1) \%$. Interestingly, the model does not always converge clearly towards the BMPP with sharp prototypical components, as shown in Fig. 16. It occurred quite often that the model solves the reasoning for the class 1 with strong negative reasoning over one component. In this case 9 components were clearly class-specific in the human understandable

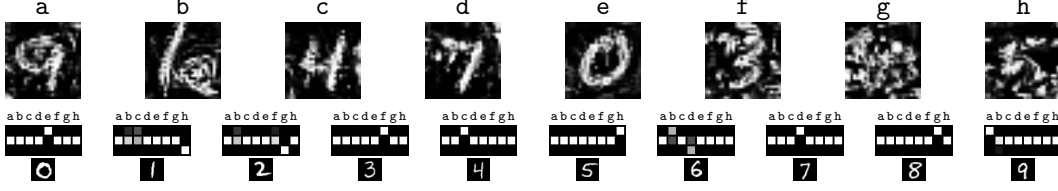


Figure 17: Learned reasoning process of a CBC with 8 components on MNIST. *Top row:* The learned components. *Bottom row:* The learned reasoning probabilities collected in reasoning matrices. The class is indicated by the MNIST digit below. The top row corresponds to $r_{c,k}^+$, middle row to $r_{c,k}^0$, and bottom row to $r_{c,k}^-$. White squares depict a probability of one and black squares of zero.

sense and the strong component for the class 1 remained in a state similar to the strong negative component in Fig. 4.

8 component CBC If we train a CBC with 8 components and compare it to the models discussed before, we can observe a slight drop in accuracy to $(99.07 \pm 0.1) \%$. To classify MNIST with only 8 components, the model learns to reason negatively over a couple of components. Similar to before, the 1 is classified via negative reasoning. In addition to that, the model classifies the 2 with negative reasoning too. In contrast to all models before, the model classifies the 6 with a combination of positive and negative reasoning. Moreover, the learned classification principle becomes hard to understand. Despite some of the components being easy to interpret, it can not be easily answered how the model uses component g for positive reasoning for class 8 and for negative reasoning for class 2.

Comparison of the models The sparsity of the number of components comes with some downsides. First of all, the models become harder to interpret as shown in the comparison between the 10 component model in Fig. 16 and the 8 component model in Fig. 17. Secondly, the networks start to classify by weaker decisions if the number of components is reduced. This is, however, not directly noticeable in the accuracy as for all three models it is still above 99%.

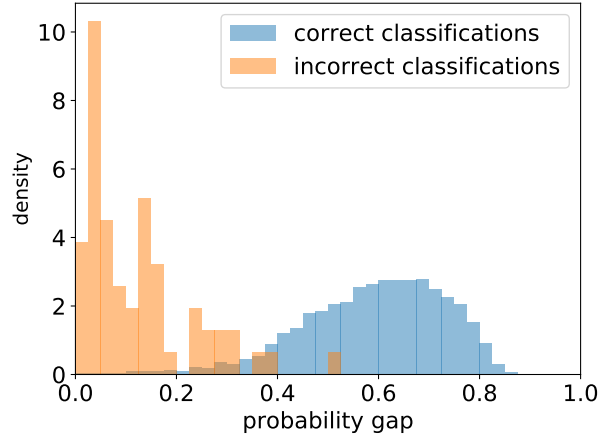
All networks are optimized towards a probability margin of 0.3 between the correct and highest probable incorrect class with the margin loss. Despite that, the 10 components network has an average probability gap of 0.59 ± 0.14 over correctly classified images after training. This shows that even though we are optimizing only for a margin of 0.3 the networks can become more discriminative by themselves and distribute the probabilities through the whole range if possible, see Fig. 18a. The figure clearly highlights that incorrectly classified images are indicated by a high uncertainty as the probability gap is much smaller. This indicates that the runner-up class and the predicted class are almost equivalent. In other words, the model is not certain about its classification decision.

If we decrease the number of components in the CBCs, we observe that the probability gap of correctly classified images becomes smaller, see the shift of the distribution in Fig. 18b and Fig. 18c. At the same time the distribution of incorrectly classified images does not change that much. Overall, the densities clearly show that the decreased number of components lowers the credibility of the model’s classification decision.

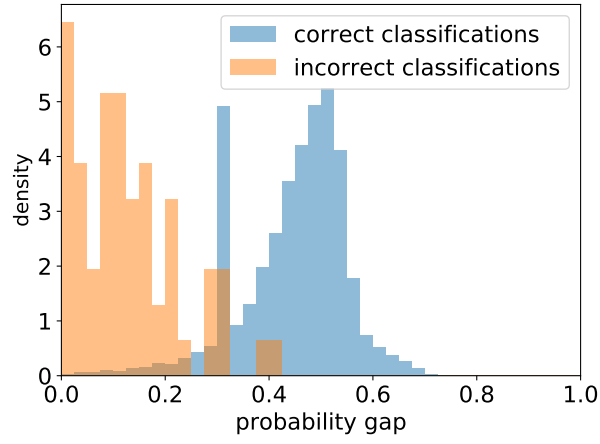
E.2.4 Adversarial robustness and rejection

During the ablation study we found that for some settings of the feature extractor, the final trained components were more interpretable than for other settings. Interestingly, the network was able to achieve close to perfect classification with both, interpretable and non-interpretable components. Given that the CBCs of the ablation study rely only on positive reasoning through the BMPP and that the components are defined in the same space as the input, we know that the components should be interpretable if $p_y(\mathbf{x}) \approx 1$ as it implies $d_k(\mathbf{x}) \approx 1$ for the prototypical component κ_k . Hence, we hypothesize: If the CBC converged to the BMPP but the trained components are not interpretable although $p_y(\mathbf{x}) \approx 1$, then it is safe to assume that the network might be susceptible for adversarial attacks.

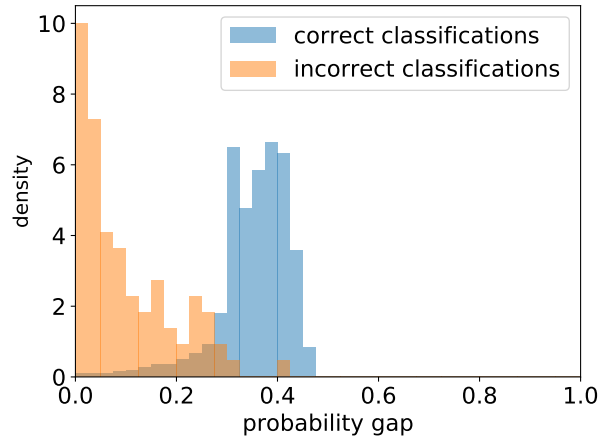
We performed a robustness evaluation to provide empirical evidence that this hypothesis is correct. Moreover, based on these results we show that the distribution of class hypothesis probabilities of



(a) 10 components CBC.



(b) 9 components CBC.



(c) 8 components CBC.

Figure 18: Distribution of the probability gap over incorrectly and correctly classified images by CBCs on MNIST with different numbers of components. We visualize discrete approximations of the continuous density functions.

Table 1: The results of the adversarial robustness evaluation. The attacks are grouped by the norm under which they are optimized, the boxes denote if the attack is either white or black box. For each model, we report the clean accuracy in %, the median- δ_a (left value) and acc- α score (right value) in % for each attack, and the worst-case analysis over all L^p -attacks by presenting the median- δ_p^* (left value) and acc- α^* score (right value) in %. Higher scores mean better robustness. For each attack the best median- δ_a is highlighted in bold.

		CNN-0		CNN-4		CBC-0		CBC-4	
	clean accuracy		99.6		99.6		98.6		99.4
L^2	DEEPFOOL \square	1.01	9.6	1.20	22.0	0.64	30.3	1.98	71.0
	C&W \square	0.86	5.2	0.99	5.1	0.58	28.5	1.27	29.6
	POINTWISE \blacksquare	2.62	88.9	2.79	93.2	1.59	53.5	3.19	94.4
	BOUNDARY \blacksquare	1.12	19.2	1.29	28.2	0.32	3.0	1.69	66.0
	worst-case	0.84	1.5	0.98	4.8	0.28	0.12	1.26	27.5
L^∞	FGSM \square	0.19	21.0	0.16	12.6	0.11	25.2	0.24	30.6
	DEEPFOOL \square	0.10	0.1	0.11	0.0	0.08	24.4	0.18	15.2
	PGD \square	0.09	6.0	0.10	2.5	0.04	1.9	0.15	0.2
	worst-case	0.09	0.0	0.09	0.0	0.04	1.9	0.15	0.02
L^0	POINTWISE \blacksquare	5.0	3.3	5.0	5.9	2.0	0.1	7.0	16.0
	S&P \blacksquare	29.0	78.0	32.0	82.2	11.0	46.6	60.0	94.2
	worst-case	5.0	3.3	5.0	5.9	2.0	0.01	7.0	16.0

a CBC can be used to detect when an image is manipulated. This property can be used for reject strategies as we show later. The same property is observed with GTSRB on real world adversarial examples, see Sec. E.3.

Network setup For the evaluation, two CBCs and two CNNs are used. The first model is equivalent to the CBC with the standard setting from the ablation study in Sec. E.2.2 with a high interpretability score of 3.8 and is called CBC-4 in the following. The second model is the equivalent CBC with the non-standard setting, which was also used previously in the ablation study in Sec. E.2.2. This model reaches an interpretability score of 0.4 and is called CBC-0.

The two CNNs are constructed by taking the feature extractor networks of the CBCs and adding two fully-connected layers on top. The fully-connected layers have 512 and 10 units respectively and are separated by a dropout of 0.5. The activation function for the first fully-connected layer is similar to the one chosen for the convolutional layers while for the final fully-connected layer the softmax activation function is used to produce a probability vector. Both networks were trained with the cross entropy loss. The other parameters of the two CNN baseline models were chosen such that CNN-0 was in line with CBC-0 and CNN-4 with CBC-4.

Robustness evaluation As the CBCs were not designed with a specific thread model in mind the robustness was evaluated over three different L^p -norms using both black and white box attacks: DEEPFOOL [55], CARLINI&WAGNER (C&W) [56], POINTWISE [57], FAST GRADIENT SIGN METHOD (FGSM) [8], BOUNDARY [46], PROJECTED GRADIENT DESCENT (PGD) [58], and SALT-AND-PEPPER noise attack (S&P) implemented in FOOLBOX [59]. We define an adversarial image \tilde{x} as a manipulated image of the input image x which is misclassified by the model. Moreover, we search for adversarial images such that $\|x - \tilde{x}\|_p$ becomes minimal. To evaluate the robustness, we tried to compute an adversary for *each* sample of the MNIST test dataset with *each* attack α and computed the adversarial distance $\delta_\alpha(x, y)$. Given a sample (x, y) from the dataset \mathcal{T} and a L^p -attack α , $\delta_\alpha(x, y)$ is defined as: **(1)** 0, if the data sample x is misclassified by the model; **(2)** $\|\tilde{x} - x\|_p$, if α found an adversary \tilde{x} ; **(3)** ∞ , if no adversary was found by α . Based on this definition we use four robustness evaluation metrics defined in [57, 60]:

Median adversarial distance: For each attack α the median- δ_α score is defined as $\text{median}\{\delta_\alpha(x, y) \mid (x, y) \in \mathcal{T}\}$, describing an averaged δ_α regarding \mathcal{T} robust to outliers.

Worst-case median adversarial distance: The median- δ_p^* score is computed for all L^p -attacks as the $\text{median}\{\delta_p^*(x, y) \mid (x, y) \in \mathcal{T}\}$, where $\delta_p^*(x, y)$ is defined as

Table 2: True positive and false positive rates for the four different rejection strategies. A threshold of $t_y = 0.4$ and $t_\beta = 0.3$ were used.

database		count	t_y	t_β	$t_y \vee t_\beta$	$t_y \wedge t_\beta$
clean images (FP)	correct classified	9 938	2.0%	3.8%	4.1%	1.7%
	incorrect classified	62	58.1%	91.9%	91.9%	58.1%
adversarial images (TP)		90 000	77.3%	99.5%	99.5%	77.3%

$\min \{\delta_a(\mathbf{x}, y) \mid \mathbf{a} \text{ is a } L^p\text{-attack}\}$. This score is a worst-case evaluation of the median- δ_a , assuming that each sample is disturbed by the respective worst-case attack \mathbf{a}_p^* (the attack with the smallest distance).

Threshold accuracy: The acc- α of a model regarding \mathcal{T} is defined as the percentage of adversarial examples found with $\delta_a(\mathbf{x}, y) > t_p$. This metric represents the remaining accuracy of the model when only adversaries below a given threshold are considered valid.

Worst-case threshold accuracy: The acc- α_p^* of a model regarding \mathcal{T} is defined as the percentage of adversarial examples found with $\delta_p^*(\mathbf{x}, y) > t_p$ using the respective worst-case attack \mathbf{a}_p^* .

Similar to [57, 60] we used the following thresholds for the evaluation: $t_0 = 12$, $t_2 = 1.5$, and $t_\infty = 0.3$.

The robustness evaluation scores are presented in Tab. 1. As highlighted in bold, for all 9 attacks (including the worst-case) the CBC-4 with interpretable components outperforms all other models by a large margin. It must also be noted that the CBC-0 model has by far the lowest robustness score across all attacks. This provides empirical evidence for the hypothesis that the interpretability of the components is a good indicator for the robustness of the CBC.

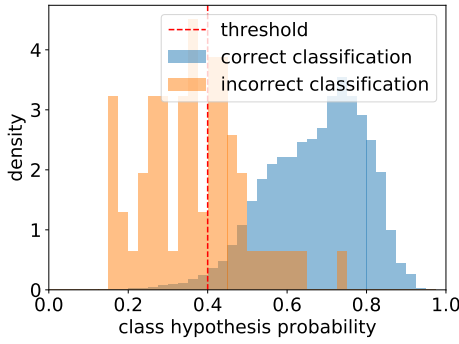
In general, the CNN baseline models have a higher robustness than the CBC-0. But in contrast to the relation between the CBC-0 and CBC-4, we observe no significant improvement in the robustness if we use the preferred feature extraction parameters in the CNN baselines. Hence, this suggest that the preferred standard setting is special to the CBCs.

Rejection of adversarial examples In Fig. 19 a collection of statistics is presented to highlight the difference between clean and adversarial examples for the CBC-4 model. Fig. 19a and Fig. 19c visualize the distribution of the predicted probability. The probability gap is visualized in Fig. 19b and Fig. 19d.

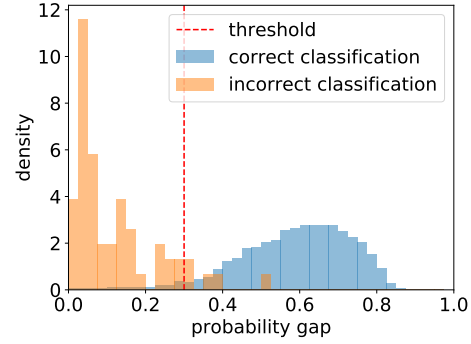
The distribution of adversarial images is similar to the distribution of incorrectly classified images. Hence, both have a significantly lower prediction probability *and* a smaller probability gap compared to correctly classified clean images. Using these two statistics, it should therefore be possible to construct a rejection strategy in which the false positives (rejected clean examples) are mostly incorrectly classified anyway. In Tab. 2 the True Positives (TP) and False Positives (FP) for four of such strategies are given. The *prediction reject strategy* rejects all inputs for which the predicted class hypothesis probability is below a probability threshold t_y . The *margin reject strategy* rejects all inputs with a probability gap below t_β . These two rejection strategies are combined, using both the logical OR and AND operations.

From Tab. 2 we can conclude that it is indeed possible to use the class hypothesis probability and the probability gap of an image to efficiently reject adversaries. Using only the margin rejection strategy with $t_\beta = 0.3$ it is possible to reject close to all (99.5% of 90 000 samples) adversarial examples generated for the CBC-4 model with only a small cost in terms of FP rate (3.8%) of correctly classified clean samples. Only using the class hypothesis probability with $t_y = 0.4$ for rejection produces an even lower FP rate (2.0%) for correctly classified clean samples but fails to reject a large portion of the adversarial examples (22.7%). Due to the excellent performance when only the class hypothesis margin is used, not a lot of benefit in terms of FP and TP rates can be gained from combining the two strategies.¹²

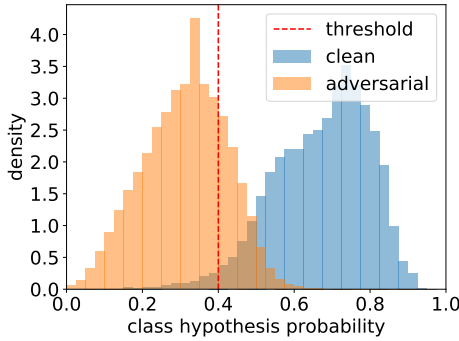
¹²For further research we want to study rejection decisions regarding the measure “probability gap times predicted class probability”.



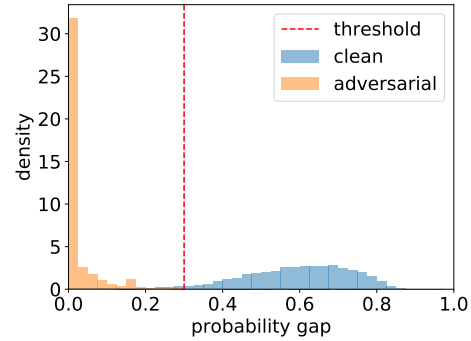
(a) The distribution of the predicted class probability for correctly and incorrectly classified clean images.



(b) The distribution of the probability gap for correctly and incorrectly classified clean images.



(c) The distribution of the predicted class probability for clean and adversarial examples.



(d) The distribution of the probability gap for clean and adversarial examples.

Figure 19: Discrete approximations of the continuous density functions of different distributions of correctly/incorrectly classified and clean/adversarial images. Additionally, we highlight the used rejection thresholds.

A clear benefit from the combination of both rejection strategies can be observed when we apply the robustness evaluation performed in the previous section over the CBC-4 model in combination with the rejection strategies. Hence, an adversarial example is only considered as valid if it is misclassified and not rejected by the strategy. We realized the generation of such adversarial examples by updating the optimization goal of the adversarial attacks to the goal of fooling the reject strategy at the same time. The FOOLBOX implementations of the C&W, DEEPFOOL, and FGSM attack were consistently not able to find an adversarial example when the OR-combined rejection strategy was used. Non-gradient based approaches, which are less restricted by the inclusion of the reject strategy, required close to double the adversarial distance to fool both the model and the reject strategy compared to the previous robustness evaluation.

E.2.5 Interpretation of the reasoning

The classification decision of a CBC can be easily interpreted. In the simplest form we can interpret the learned reasoning process by visualizing the reasoning probabilities and/or the learned components, as we showed multiple times before, e. g. in Sec. 4.1.1. If the CBC uses patch components, see Sec. 2.2, then it is also possible to visualize the learned model using heatmaps and reconstructions. We will focus in the following on the creation of these visualization and how they relate to the probabilistic model. While this section primarily focuses on the patch components setting, the visualization techniques can partly be applied to full-size component CBC, even when the components are not defined in the input space. By taking advantage of the similarity properties in use, we can construct further interpretation techniques, as was shown in Sec. E.2.2.

In this section, the same CBCs with patch components and spatial reasoning as in Sec. 4.1.2 are used. Again, they are denoted as α -CBC and \varnothing -CBC. In general, the models follow the Siamese architecture depicted in Fig. 3 except that we apply a max pooling operation of pool size and stride 3×3 after the detection probability measuring to downsample the detection possibility stack to a size of $v_d, h_d = 7$. Both models share the same feature extractor of:

1. Convolution: 32 filters, kernel size 5×5 , stride 1×1 , bias, no padding;
2. Convolution: 64 filters, kernel size 3×3 , stride 1×1 , bias, no padding.

The 8 patch components are defined as 7×7 patches ($v_\kappa, h_\kappa = 7$) in the input space. Hence, the feature stacks have a size of $v'_x, h'_x = 22$ and $v'_\kappa, h'_\kappa = 1$ after the feature extraction. We applied multiple reasoning with two reasoning stacks per class and increased the number of training epochs to 300 accordingly. All other parameters, the training procedure and the initialization, are equivalent to the standard setting. The α -CBC has trainable pixel probabilities $\alpha_{c,i,j}$ and the \varnothing -CBC has non-trainable, fixed pixel probabilities defined as $\alpha_{c,i,j} = 1/(v_r \cdot h_r)$.

Theoretical basis of the visualizations All visualizations show the learned reasoning process and, hence, the weights of the probability model. More precisely, we visualize the effective reasoning probabilities $\bar{\mathbf{r}}_c^\pm$ in two different ways. First, as input independent visualizations without the interaction with a given input. Second, as input dependent visualizations with interaction with a given input. CBCs compute the final probability output $p_c(\mathbf{x})$ for a class c by Eq. (1) as the probability of agreement A under the condition of importance I , see Sec. B.1, abbreviated by $A|I$:

$$P(A|I, \mathbf{x}, c) = (\mathbf{d}(\mathbf{x}))^T \cdot \bar{\mathbf{r}}_c^+ + (\mathbf{1} - \mathbf{d}(\mathbf{x}))^T \cdot \bar{\mathbf{r}}_c^-.$$

This equation can be split into positive agreement under the condition of importance ($A^+|I$)

$$P(A^+|I, \mathbf{x}, c) = (\mathbf{d}(\mathbf{x}))^T \cdot \bar{\mathbf{r}}_c^+,$$

and negative agreement under the condition of importance ($A^-|I$)

$$P(A^-|I, \mathbf{x}, c) = (\mathbf{1} - \mathbf{d}(\mathbf{x}))^T \cdot \bar{\mathbf{r}}_c^-.$$

Both entities resemble probabilities in favor of the class c . Particularly, $P(A^+|I, \mathbf{x}, c)$ is the probability in favor of class c by components that have been detected and that should be detected (positive reasoning), and $P(A^-|I, \mathbf{x}, c)$ is the probability in favor of class c by components that have been not detected and that should be not detected (negative reasoning). Additionally, we can compute the probability against a class c by disagreement \bar{A} under the condition of importance I , abbreviated by $\bar{A}|I$:

$$\begin{aligned} P(\bar{A}|I, \mathbf{x}, c) &= 1 - P(A|I, \mathbf{x}, c), \\ &= (\mathbf{1} - \mathbf{d}(\mathbf{x}))^T \cdot \bar{\mathbf{r}}_c^+ + (\mathbf{d}(\mathbf{x}))^T \cdot \bar{\mathbf{r}}_c^-. \end{aligned}$$

This equation can be split into positive disagreement under the condition of importance ($\bar{A}^+|I$)

$$P(\bar{A}^+|I, \mathbf{x}, c) = (\mathbf{1} - \mathbf{d}(\mathbf{x}))^T \cdot \bar{\mathbf{r}}_c^+,$$

and negative disagreement under the condition of importance ($\bar{A}^-|I$)

$$P(\bar{A}^-|I, \mathbf{x}, c) = (\mathbf{d}(\mathbf{x}))^T \cdot \bar{\mathbf{r}}_c^-.$$

$P(\bar{A}^+|I, \mathbf{x}, c)$ can be interpreted as the probability against the class c by components that have been not detected and that should be detected. Similar to that, is the interpretation of $P(\bar{A}^-|I, \mathbf{x}, c)$. It is the probability against class c by components that have been detected and that should be not detected. These four probabilities are the main ingredients for the visualizations and are related to paths in the probability tree diagram T , see Fig. 2 for a sub-tree T_c of T .

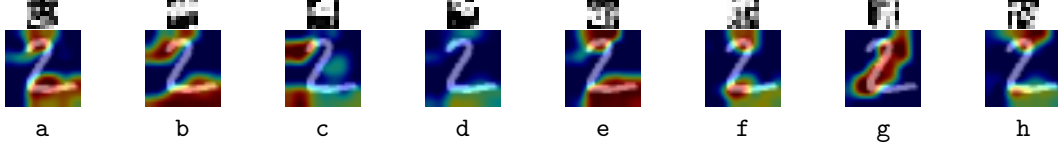


Figure 20: Detection probability heatmaps of the α -CBC on a test sample. At the top of each heatmap we depict the respective patch component. We use the color coding “JET” to map probabilities of 0 to blue and 1 to red.

Detection heatmap visualizations We can use the detection probability function $d_k(\mathbf{x})$ for a certain component κ_k to get an indication where a component had a detection in the input. We visualize all eight detection probability heatmaps for the α -CBC over a test input in Fig. 20. If we consider component b, then we see that it models almost a horizontal stroke. This is reflected in the heatmap showing that the horizontal lines of the two have a high detection to this component. Since the horizontal stroke is modeled in the upper part of the patch it might appear in the heatmap that the detection of the stroke is in a lower region and moreover has a slight offset. As another example, consider component g. This component is almost a vertical line and correctly detects the vertical part of the two. In contrast, the component d models the lower left part of a circle and, hence, has no similarities with parts within the sample.

The detection heatmaps are useful to gain an understanding of the similarity measure, especially if the representation of the components are learned in the input space and are interpretable. If this is not the case, then it could become hard to understand what a component really encapsulates. In this case applying a back projection strategy like in the IMAGENET experiment can be useful, see Sec. 4.2.

Incorporation of pixel probabilities If spatial reasoning is used, the pixel probabilities have to be incorporated in the visualizations. The pixel probabilities indicate how important a pixel position i, j is for the class c . Moreover, they determine how to combine the single $p_{c,i,j}(\mathbf{x})$ for the class output $p_c(\mathbf{x})$. We include the pixel probabilities by a final scaling step applied to the reasoning heatmaps and reconstructions defined by:

1. Collect all the pixel probabilities $\alpha_{c,i,j}$ for one class c into a map.
2. Normalize the map by $\max_{i,j} \alpha_{c,i,j}$.
3. Upsample the map to the respective size of the target map (e. g. a heatmap).
4. Multiply the resized map with the target map.

Reasoning heatmap: input independent visualizations To answer the question “What has a model learned about a certain class c ?” we consider input independent heatmaps. The idea is to stimulate the effective reasoning possibility vectors $\bar{\mathbf{r}}_c^\pm$ by the optimal detection possibility vector and highlight the regions in favor of class c from the positive and negative reasoning perspective. The optimal detection possibility vector for $A^+|I$ is $\mathbf{d}(\mathbf{x}) = \mathbf{1}$ and, moreover, $\mathbf{d}(\mathbf{x}) = \mathbf{0}$ for $A^-|I$. By using these optimal inputs we compute the reasoning heatmaps for a class c by:

1. Upsample the $v_r \times h_r \times \#\mathcal{K}$ effective reasoning possibility stacks to $v_x \times h_x \times \#\mathcal{K}$.
2. Compute the pixel-wise dot product with the respective optimal detection possibility vector to obtain the heatmap of size $v_x \times h_x$.
3. Overlay the pixel probability map.

By these maps we find the regions for a model where components have to be and have to be not detected. Consider Fig. 21 where we visualize the learned concepts for both models. Fig. 21a shows the learned sparse encodings of the α -CBC. For example for class 3, the model learns to classify the digit by recognizing specific line endings. In contrast, the class 1 is classified with negative reasoning only by checking that no component matches around the vertical stroke.

In Fig. 21b we depict the reasoning heatmaps for the non-trainable pixel probabilities model \emptyset -CBC. Since all $\alpha_{c,i,j}$ are equivalent, the final overlay of the pixel probability maps does not change the

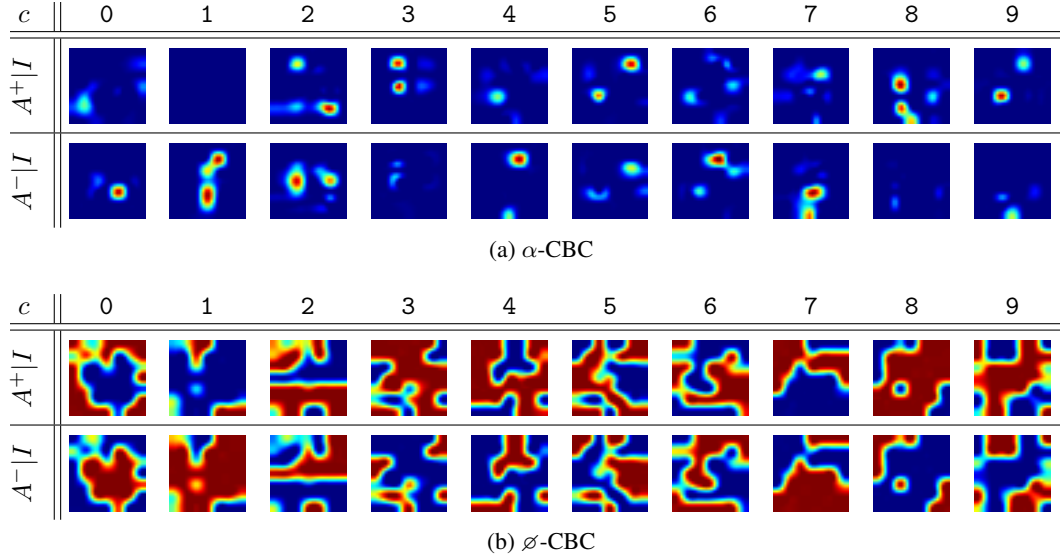


Figure 21: Input independent reasoning heatmaps for α -CBC and \emptyset -CBC for all classes. For each class, we depict one reasoning stack. Class labels are shown at the top. We use the color coding “JET” to map probabilities of 0 to blue and 1 to red.

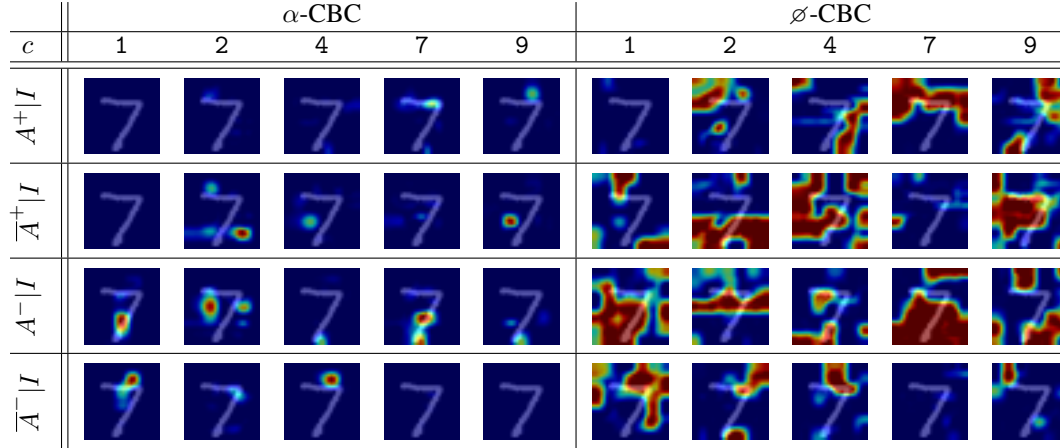


Figure 22: Input dependent reasoning heatmaps of α -CBC and \emptyset -CBC for certain classes and for a test sample (class 7) from the MNIST database. We use the color coding “JET” to map probabilities of 0 to blue and 1 to red.

visualizations as each pixel probability has the same importance. Moreover, the model is forced to reason correctly over each position to reach a high output probability. By the probability model, the sum over positive and negative effective reasoning has to be one. Hence, $A^+|I$ and $A^-|I$ are complementary to each other. The reasoning heatmaps can be hard to interpret as they might highlight background with positive reasoning in case a background component was learned. If we consider the learned concept of the class 0, then we see how the model detects the outer shape of the zero with $A^+|I$ and the black middle with $A^-|I$. Another good example is the class 4. The shape of a four is clearly visible in the $A^+|I$ heatmap and via $A^-|I$ it looks at the top and bottom that nothing is detected there to avoid confusions to other digits like a nine.

Reasoning heatmap: input dependent visualizations The input dependent heatmaps are constructed in the same way as the input independent heatmaps except that we take as possibility vector the detection possibility vector from the respective position of the detection possibility stack $\mathbf{d}(\mathbf{x})$.

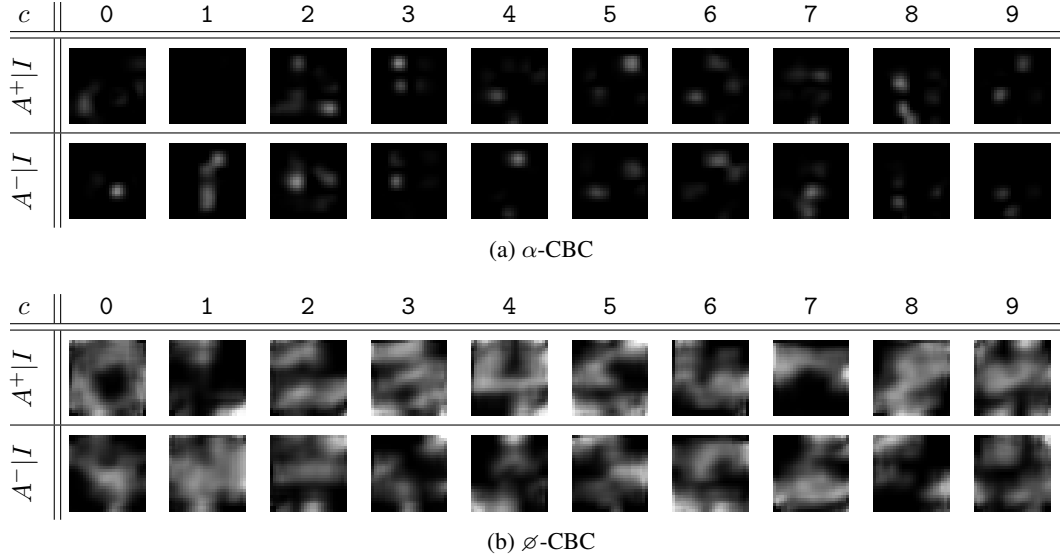


Figure 23: Input independent reasoning reconstructions for α -CBC and \emptyset -CBC for all classes. For each class we depict one reasoning stack. Class labels are printed at the top.

Additionally, we highlight the input image in the background. Now, we can visualize $A^\pm|I$ and $\bar{A}^\pm|I$ resulting in four possible visualizations.

Consider Fig. 22 where we took a test sample from the MNIST database and show for five classes which parts provided evidence in favor of or against the class decision. In combination with the optimal heatmaps of Fig. 21 we can see where the decision of the respective class diverges from the optimum. For example, the α -CBC requires for an input to be classified as a two, that it detects the top arc ending, the significant bottom left corner, and the bottom line ending. The failure of the model to detect these features is depicted by the $\bar{A}^+|I$ heatmap highlighting the areas where these features should be detected to support the decision of a two. Nevertheless, the model highlights in the $A^-|I$ heatmaps, that the negative reasoning requirements are fulfilled to be classified as a two. In contrast, if we consider the $A^+|I$ and $A^-|I$ heatmaps of class 7 we see that all requirements are fulfilled to be a seven, which is the correct output class. For this correct class almost no $\bar{A}|I$ is observed. Note for other classes, like the class 9, how the heatmaps correctly highlight the common features of the two classes.

The behavior of the \emptyset -CBC is similar to the α -CBC except that it requires a correct reasoning over the whole image instead of reasoning over a few regions. First, note how the combination of the $A^\pm|I$ and $\bar{A}^\pm|I$ heatmaps for one class result in the respective input independent heatmap of Fig. 21. Consider the class 4 of the \emptyset -CBC. The $A^+|I$ heatmap highlights correctly that the vertical stroke of the seven could be the vertical stroke of a four too. Hence, the method reasons in favor of class 4 over this part of the digit. Nevertheless, it highlights in the $\bar{A}^+|I$ heatmap that the left part of the four is not detected. Additionally, the important sanity check that there is no top stroke at a four fails as it is clearly highlighted in the $\bar{A}^-|I$ heatmap. Overall the heatmaps of this class highlight a lot $\bar{A}|I$ for the classification decision of a four. In contrast, there is close to no $\bar{A}|I$ for the correct class and, hence, the input is correctly classified as a seven.

Reasoning reconstruction: input independent visualizations The reconstructions are similar to the heatmaps with the difference that we incorporate the learned patch components. A requirement for this visualization technique is that the components are defined in the input space. Moreover, we assume that the input space was defined over $[0, 1]$. Again we use the optimal detection possibility vectors and do the reconstruction by:

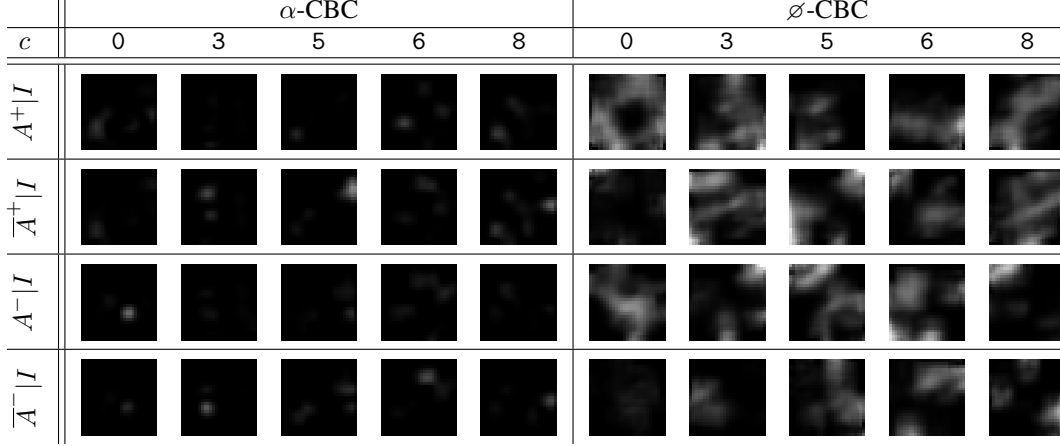


Figure 24: Input dependent reasoning heatmaps of α -CBC and \emptyset -CBC for certain classes and for the third test sample (class 0) from the MNIST database.

1. Initialize a zero matrix of size $(v_r + v_\kappa) \times (h_r + h_\kappa)$ as target image.¹³
2. For each pixel position i, j in $v_r \times h_r$ and component κ_k do:
 - (a) Scale the component κ_k by the probability i, j, k from the effective reasoning possibility stack.
 - (b) Add the scaled component of size $v_\kappa \times h_\kappa$ to the target image at the corresponding receptive field, which is the area $i, i + 1, \dots, i + v_\kappa - 1$ and $j, j + 1, \dots, j + h_\kappa - 1$.
3. Normalize each intensity value in the target image by the overall count, that a filter of size $v_\kappa \times h_\kappa$ has covered that pixel when it was slid over the target image.
4. Overlay the pixel probability map.

The visualizations which are obtained by this principle visualize the same information that are included in the corresponding heatmaps. Hence, it is just a different way of visualizing the learned concepts. The advantage is that the reconstructions for the \emptyset -CBC are easier to interpret. For example, Fig. 23b clearly shows digit shapes in $A^+|I$ for the most classes. Moreover, the learned sanity checks by $A^-|I$ becomes easier to understand. For the class 3 the model checks that the ends of the three are not closed, which is an important difference to an eight. In contrast to the heatmaps, the overlay of $A^+|I$ and $A^-|I$ does not result in a white image as we incorporated the components which could consist of black regions or not perfectly white shapes.

On the contrary, the α -CBC reconstructions are pretty much black images with white blobs. It underlines the strong sparse coding which is learned for MNIST. For example, the classification of a six is based on the recognition of the intersection between the lower and the upper part, the top line ending, and that there is no line which connects the upper ending with the lower circle (to distinguish to an eight).

Reasoning reconstruction: input dependent visualizations Similar to the heatmaps, we obtain this visualizations by exchanging the optimal possibility vector with the detection possibility vector from the respective position of the detection possibility stack $\mathbf{d}(\mathbf{x})$. Beside that we follow the algorithm for input independent reconstructions. In Fig. 24 we show the reconstructions of a test sample from the MNIST database. In accordance to that, we show the reconstructions for those classes which were not depicted in Fig. 22. Both models do a correct prediction as we see in the $\bar{A}^\pm|I$ reconstructions. Nevertheless, how they achieve this is highly different and we leave it to the interested reader to start an interpretation why the models did not classify the input as another digit.

Summary In the previous paragraphs, we studied the interpretability of patch models with spatial reasoning using two different models. With an accuracy of $(97.33 \pm 0.19)\%$ the models perfor-

¹³It is possible to upsample the reasoning stack first to get a higher resolution in the target image. We upsampled first to a size of $v'_x \times h'_x \times \#\mathcal{K}$ which results in a target image of $v_x \times h_x$.

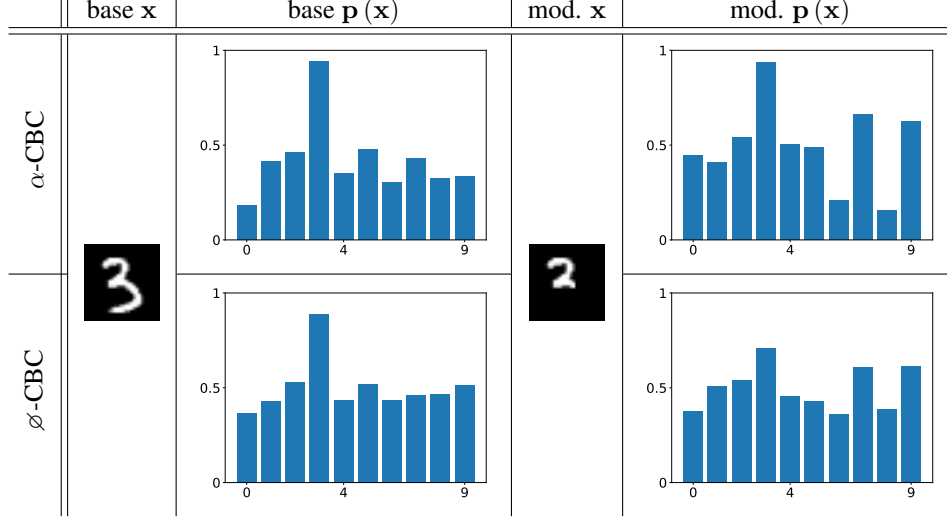


Figure 25: Results of the cut-off experiment where we modified a base image regarding the import regions marked by $A|I$ heatmaps.

mance is considerably lower than the state-of-the-art. One reason might be that the models we used are quite sparse. Both have only 35 K trainable parameters. The accuracy can be increased towards state-of-the-art if we use a deeper feature extractor. A problem that emerges in this case is that the receptive field and moreover the minimal size for patches increases too as the receptive field size is the minimal patch size. Of course, this is not a problem in general but it was obstructive in the experiments. If we increase the network depth and, moreover, the patch size, then the network starts to rely mostly on positive reasoning and, moreover, in some cases the reconstructions become less meaningful. However, the goal of this section was to show that the model classifies by using negative reasoning and that the reconstruction principle works. Hence, we decided to accept the low accuracy models.

The reconstructions of inputs via back projecting the components seems to be a visualization that should work in principle. However, till now we neither got it working to acceptable results on colored datasets nor on deep networks with more than 4-layers. The reason for that is not clear so far and we hope that we can improve these results in the future.

The heatmaps and the detection probability maps are applicable independently to the space where the components are trained and, hence, provide a powerful tool to gain insights of the learned reasoning process. To provide evidence that these visualizations are really showing the learned concepts, we present in the main part of the paper the visualizations with an adversarial image. The idea behind this experiment is to make a stress test of the evaluations by explaining “Why does the adversary fool the model?” In parallel to that, we can do an even more aggressive stress test: Because of Fig. 21 and Fig. 23 we know exactly which regions of a given digit are the most important parts for a certain classification. Hence, if the visualizations are correct, then it should be possible to remove all the unimportant parts without effecting the classification decision. Consider Fig. 25 where we visualize the results of such an experiment for both models. We used the same inputs for both models. The input sample is an image from the test sample database. Without any special tuning, we removed the parts of a three which are not marked as important by the α -CBC see Fig. 21. As we see in the base $\mathbf{p}(\mathbf{x})$ distributions both models classify the original input image correctly but the α -CBC predicts a more confident classification as the margins to other classes are higher. If we remove parts of the input which are highlighted to not contribute to the class decision of the α -CBC for a three we observe no real drop in the output probability even though the probability for other classes changes. The image is still classified as a three even though it looks more like a small two. In contrast to the α -CBC, the \emptyset -CBC realizes the manipulation as the probability drops but still classifies the image as a three. This is because in the \emptyset -CBC each pixel position contributes equally and, hence, every part of the three is important as shown in Fig. 23. This again underlines the descriptive power of the visualization techniques.

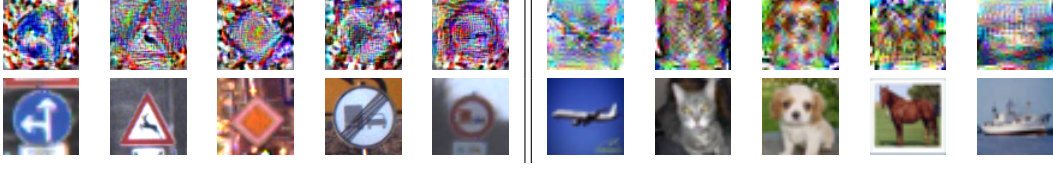


Figure 26: Visualizations of five learned components on GTSRB (left) and CIFAR-10 (right). *Top row*: The learned components. *Bottom row*: Similar training sample \mathbf{x} for each κ_k regarding $d_k(\mathbf{x})$.

With the α -CBC and \varnothing -CBC, we proposed two different models which behave totally different in classifying the data. The α -CBC can classify the data by only reasoning over a few pixel positions. We consider this model type as an example of how usual NNs classify as we usually do not constrain a NN regarding how much of the image has to be understood. In contrast, the \varnothing -CBC is constrained to understand the whole image as each pixel position contributes equally. Right now, we are not sure what is the superior method (if there is one) or if a trade-off between both via a regularization of $\alpha_{c,i,j}$ is the right way to go. Remarkably, we have the feeling that the \varnothing -CBC could be the better method to detect outliers or manipulation in images, as in the experiments they always resulted in a drop of the probability $p_y(\mathbf{x})$ and the margin to the runner-up class (see also Fig. 5).

E.3 GTSRB

In this experiment, we evaluate the performance and robustness of the CBC compared to a baseline CNN on GTSRB [61]. This is done to show that CBCs scale to RGB images with background noise where one class can be represented by a prototype. The 4-layer CNN feature extractor of the 43 components CBC is slightly different to the one used on MNIST:

1. Convolution: 32 filters, kernel size 7×7 , stride 1×1 , bias, no padding;
2. Convolution: 64 filters, kernel size 3×3 , stride 1×1 , bias, no padding;
3. Max pooling: pool size and stride 2×2 ;
4. Convolution: 64 filters, kernel size 5×5 , stride 1×1 , bias, no padding;
5. Convolution: 128 filters, kernel size 3×3 , stride 1×1 , bias, no padding.

The overall setting of the CBC is the standard setting for a CBC. We trained the network over increasing margins in three steps starting with $\beta = 0.1$ and increasing to $\beta = 0.2$ and $\beta = 0.3$. If trained from the beginning with the target margin of 0.3, the model converges to a local minima of low accuracy. In this case, the model does not learn a strong positive component for each class. Moreover, some components resemble the same class. With only 43 components for 43 classes and the applied BMPP, this makes it impossible to correctly classify each class. We trained with each of the margins for 150 epochs. The images were rescaled to $v_x, h_x = 64$ and normalized to $[0, 1]^{64 \times 64 \times 3}$ by the following procedure:

1. Normalize each image by the mean and standard deviation.
2. Clip the normalized image to the interval $[-2, 2]$.
3. Project the resulted image back to $[0, 1]^{64 \times 64 \times 3}$.

The baseline CNN is constructed by replacing the detection probability and reasoning layer by a classic convolution and a fully-connected layer such that the CBC and the baseline CNN are architectural equivalent. To be more exact, the baseline CNN is obtained by applying the following two layers after the feature extraction:

1. Convolution: 43 filters, kernel size 22×22 , stride 1×1 , bias, no padding, ReLU;
2. Fully-connected: 43 neurons, softmax.

We trained the baseline CNN with the cross entropy loss for 450 epochs and with an initial learning rate of 0.0001. All other parameters are equivalent to the non-standard CBC setting.

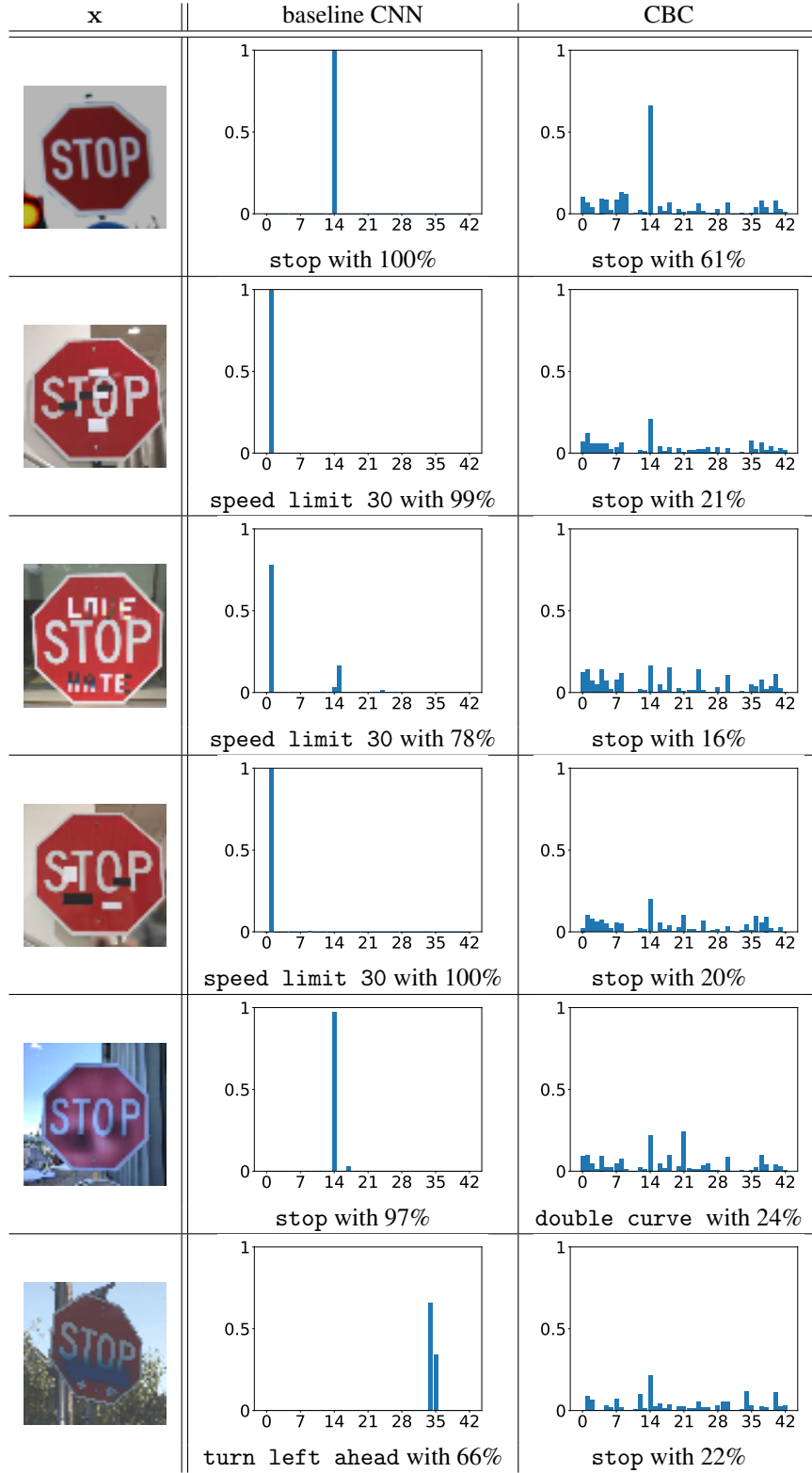


Figure 27: Physical stop sign adversaries applied to the baseline CNN and to the CBC. The input x and the corresponding output distribution $p(x)$ are depicted. Additionally, the predicted label with the corresponding prediction probability are presented below each distribution. The first image is a sample from the GTSRB test database and shows the probability distribution of both models on a clean image.

Both networks achieve a comparable accuracy of $(97.2 \pm 0.77) \%$ for the CBC and $(97.5 \pm 0.18) \%$ for the baseline CNN. The trained CBC has a distribution of the probability gap similar to the 10 component CBC trained on MNIST. The average probability gap is 0.58 ± 0.17 . In contrast, the baseline CNN has an average probability gap of 1 ± 0.03 and, hence, is almost returning a one-hot coding. As shown in Fig. 26 the trained CBC has interpretable components and classifies by the BMPP. In contrast to MNIST, we observed stronger variations in the components between the different runs. For example the background noise was highly varying. But in general, the components were always interpretable.

To underline the initial robustness evaluations performed on MNIST (see Sec. E.2.4), we tested the robustness of the CBC and the baseline CNN on the physical stop sign adversaries from [50]. The resulting behavior on these images is similar to the robustness results on MNIST. The CBC has no tendency to be overconfident, see Fig. 27. The CBC is not classifying all the adversaries correctly, but it does not predict an overconfident output probability either. Moreover, compared to the probability distribution on the clean input, we see a clear difference to the probability distributions of the adversaries. All probabilities drop and the model is clearly uncertain about its decision. This result is aligned to the observed behavior on MNIST and can be a promising property for further research in the field of outlier detection / rejection.

E.4 CIFAR-10

Compared to GTSRB, CIFAR-10 [62] is harder to classify as the single classes cannot be represented by a single prototype due to large within-class variations and heavier background noise. We used a CBC with 10 full-size components and the standard setting, as found during the ablation study in Sec. E.2.2. To train on CIFAR-10, we changed the initialization strategy of the components. The 10 components are now initialized by using the 10 class means. Moreover, at the beginning we trained with the mean squared error over $\mathbf{p}(\mathbf{x})$ for 25 epochs against a one-hot class label vector. This helps the model to become discriminative. If trained over the mean squared error only, the network starts to converge to local minima of lower accuracies of $\approx 73\%$. After the initial few epochs, we switched to the training strategy used for GTSRB with increasing margins and an initial learning rate of 0.001. Again, the baseline CNN is the architectural equivalent of the CBC with the following layers after the feature extraction:

1. Convolution: 10 filters, kernel size 5×5 , stride 1×1 , bias, no padding, ReLU;
2. Fully-connected: 10 neurons, softmax.

The baseline CNN was trained with the cross entropy loss for 475 epochs and an initial learning rate of 0.001. All other parameters are equivalent to the non-standard CBC setting.

As expected, the CBC started to classify by the BMPP and formed prototypical components. We visualized five components in Fig. 26. The components show different common characterizing attributes of the classes, such as: texture (e.g. fur of the cat), rough shapes (e.g. main shape of the horse), important arrangements of features (e.g. ears, eyes, and snout of the dog), the general dominating colors at certain positions (e.g. white and blue for the ship), etc. Across all runs, the learned components looked almost equivalent.

The CBC achieves an accuracy of $(77.2 \pm 0.07) \%$ and the baseline CNN of $(79.9 \pm 0.3) \%$. Hence, the performance of both networks is almost at the same level. The probability distribution over the test dataset shows that the CBC has a much smaller average probability gap with $(0.29 \pm 0.17) \%$ than we observed for MNIST and GTSRB. This is also reflected in the low accuracy compared to state-of-the-art results. The fact that we had no success to “easily” train on CIFAR-10 in the same fashion in which we did on GTSRB, is a good indicator that the loss function might not be suitable in general and can be improved.